# ELECTRON TUNNELING MEASUREMENTS ON FERROMAGNETICALLY DOPED LANTHANUM MANGANITE FILMS

By

HEATHER D. HUDSPETH

A DISSERTATION PRESENTED TO THE GRADUATE SCHOOL OF THE
UNIVERSITY OF FLORIDA IN PARTIAL FULFILLMENT OF THE REQUIREMENTS
FOR THE DEGREE OF DOCTOR OF PHILOSOPHY

UNIVERSITY OF FLORIDA

2000

I would like to dedicate this dissertation to my husband, Quentin.
Without his loving support I would have never gotten this far. Thanks, Q.

# ACKNOWLEDGMENTS

I would like to thank all the people who have helped me achieve my goal of becoming a doctor. In particular, I wish to thank my advisor, Fred Sharifi. I am sincerely grateful for all his encouragement, advice, and support. Special thanks go to Peng Xiong and Stephen von Molnar for the thin films used in the study as well as for all the helpful discussions. Many thanks go to Selman Hershfield, Arthur Hebard, Stephen Pearton, Christopher Stanton, and Mark Meisel for serving on my supervisory committee at one time or another.

I am always grateful for the encouragement of my husband, parents, family, and friends. I would never have achieved my successes without all their love and support. I would especially like to thank my Dad, Jeff Lynn, for the critical reading of this dissertation.

# TABLE OF CONTENTS

page

ACKNOWLEDGMENTS ........ iii

TABLE OF CONTENTS ........ iv

LIST OF FIGURES ........ vi

ABSTRACT ........ viii

CHAPTERS

1 INTRODUCTION ........ 1

2 TUNNELING SPECTROSCOPY ........ 4

- 2.1 Metal-Insulator-Metal Tunnel Junctions ........ 4
  - 2.1.1 $T = 0$ Steady-State Calculation ........ 8
  - 2.1.2 $T \neq 0$ Steady-State Calculation ........ 9
- 2.2 Metal-Insulator-Superconductor Tunneling ........ 10
- 2.3 Schottky Barrier Effects ........ 13

3 REVIEW OF $La_{1-x}(Ca, Sr)_xMnO_3$ ........ 18

- 3.1 Crystal Structure ........ 18
- 3.2 Phase Diagram ........ 21
- 3.3 Colossal Magnetoresistance ........ 23
- 3.4 Double Exchange ........ 24
- 3.5 Jahn-Teller Distortion ........ 28
- 3.6 Electron-Lattice Coupling ........ 30
- 3.7 Band Structure ........ 31

4 REVIEW OF EXPERIMENTAL EVIDENCE ........ 33

- 4.1 Transport and Thermodynamic studies ........ 33
  - 4.1.1 Low Temperature Resistivity ........ 34
  - 4.1.2 High Temperature Resistivity and Thermopower ........ 34
  - 4.1.3 Specific Heat ........ 35

4.1.4 Thermal Conductivity ....................35
4.1.5 Isotope Effect ....................36
4.1.6 Optical/Raman Spectroscopy ....................36
4.2 Structural Experiments ....................37
4.2.1 EXAFS ....................37
4.2.2 Neutron Scattering ....................38
4.2.3 Neutron Scattering Pair Density-Function Analysis ....................39
4.3 Previous Tunneling Experiments ....................39
4.3.1 Scanning Tunneling Spectroscopy ....................41
4.3.2 Trilayer Tunneling Spectroscopy ....................41

5 FABRICATION ....................43

5.1 Film Characterization ....................43
5.2 Tunnel Junction Preparation ....................46
5.2.1 Ion-milled Barrier ....................47
5.2.2 Chemically Formed Barrier ....................52

6 DATA ACQUISITION ....................54
6.1 Measurements ....................54
6.2 Junction Quality ....................58
6.3 $La_{0.67}Ca_{0.33}MnO_3$ Tunneling Results ....................64
6.3.1 Zero-Bias Conductance Measurements ....................64
6.3.2 Low Temperature Conductance Measurements ....................69
6.3.3 Middle Temperature Conductance Measurements ....................72
6.3.4 High Temperature Conductance Measurements ....................75
6.4 Preliminary $La_{0.67}Sr_{0.33}MnO_3$ Tunneling Results ....................77
6.4.1 Zero-Bias Conductance Measurements ....................77
6.4.2 Low Temperature Measurements ....................80

7 SUMMARY ....................82

REFERENCES ....................84

BIOGRAPHICAL SKETCH ....................87

# LIST OF FIGURES

Figure page

2.1 Sketch of a cross-stripe tunnel junction ....5

2.2 T = 0 Energy diagram of a NIN tunnel junction ....7

2.3 T = 0 Energy diagram of a SIN tunnel junction ....11

2.4 T = 0 I vs. V sketch of a superconductor ....12

2.5 T = 0 Energy diagram of a SIN junction with a Schottky barrier ....14

2.6 Schottky barrier sketch with different applied voltages ....15

2.7 Sketch of a Schottky barrier profile for different resistance junctions ....16

2.8 Sketch of a G vs. V plot for different resistance junctions ....17

3.1 Sketch of an undistorted perovskite structure ....19

3.2 $La_{1-x}Sr_xMnO_3$ resistance vs. temperature graph ....25

3.3 $La_{1-x}Sr_xMnO_3$ magnetization vs. temperature graph ....26

3.4 Energy diagram of the effects of Jahn-Teller distortions ....29

5.1 $La_{1-x}Ca_xMnO_3$ R vs. T graph ....44

5.2 $La_{1-x}Ca_xMnO_3$ M vs. T graph ....45

5.3 Sketch of sample before barrier formation ....47

5.4 I vs. V graph comparing Ar and Xe barriers, T = 2 K ....50

5.5 G vs. V graph comparing Ar and Xe barriers, T = 2 K ....51

5.6 G vs. V graph comparing Xe and Br-etched barriers, T = 43 K ....53

6.1 Circuit diagram used to measure tunneling I as a function of V ....55

6.2 Circuit diagram used to measure tunneling G as a function of V .................. 57

6.3 Typical I and G vs. V graphs, T = 2 K .................. 59

6.4 G vs. V graph for different resistance junctions, T = 10 K .................. 61

6.5 Exponential fit of conductance data for V > 100 mV, T = 10 K .................. 62

6.6 T = 0 BCS fit to G vs. V graph, T = 2 K .................. 63

6.7 $La_{1-x}Ca_xMnO_3$ Zero bias G vs. T graph, T = 20 K- 290 K .................. 65

6.8 $La_{1-x}Ca_xMnO_3$ Zero bias G vs. T graph, T = 4 K - 140 K .................. 67

6.9 $La_{1-x}Ca_xMnO_3$ G vs. V graph, T = 2 K - 265 K .................. 68

6.10 $La_{1-x}Ca_xMnO_3$ G vs. V graph, T = 8 K - 30 K .................. 70

6.11 Normalized $La_{1-x}Ca_xMnO_3$ G vs. V graph, T = 10 K - 40 K .................. 71

6.12 $La_{1-x}Ca_xMnO_3$ G vs. V graph, T = 33 K – 80 K .................. 73

6.13 Normalized $La_{1-x}Ca_xMnO_3$ G vs. V graph, T = 10 K– 80 K .................. 74

6.14 $La_{1-x}Ca_xMnO_3$ G vs. V graph, T = 150 K – 265 K .................. 76

6.15 $La_{1-x}Sr_xMnO_3$ Zero bias G vs. V graph, T = 4 K – 190 K .................. 78

6.16 $La_{1-x}Sr_xMnO_3$ G vs. V graph, T = 10 K– 250 K .................. 79

6.17 $La_{1-x}Sr_xMnO_3$ G vs. V graph, T = 10 K - 30 K .................. 81

Abstract of Dissertation Presented to the Graduate School
of the University of Florida in Partial Fulfillment of the
Requirements for the Degree of Doctor of Philosophy

# ELECTRON TUNNELING MEASUREMENTS ON FERROMAGNETICALLY DOPED LANTHANUM MANGANITE FILMS

By

Heather D. Hudspeth

May 2000

Chairman: Fred Sharifi
Major Department: Physics

A series of tunneling and transport measurements on $La_{0.67}Ca_{0.33}MnO_3$ and $La_{0.67}Sr_{0.33}MnO_3$ perovskite thin films is presented. Planar tunnel junctions were fabricated using the manganite thin film as one electrode. To ensure a high-quality tunnel junction, a well-characterized superconductor, Pb, is used as the other electrode. Below the Pb superconducting transition temperature, $T_c$, the associated superconducting gap and phonon structures are fully observed. Measurements of tunneling current and conductance as a function of bias voltage were obtained for temperatures ranging from 2 K to 300 K.

For $La_{0.67}Ca_{0.33}MnO_3$, our tunneling measurements show the density of electronic states at the Fermi level increasing slowly below 250 K, the ferromagnetic ordering temperature of the $La_{0.67}Ca_{0.33}MnO_3$ film. Carrier mobility plays a dominant role in electron transport as the material undergoes a ferromagnetic metal-insulator transition at

250 K. Our measurements are consistent with a Fermi level moving through a mobility edge as this material orders ferromagnetically. Below 40 K, we see a depletion in the density of states centered at the Fermi level and extending a few meV. The results are consistent with a depletion of one spin band. We also see evidence for inelastic excitations in the density of states over a broad energy range. We attribute these excitations to polaronically localized electrons coexisting with mobile carriers in the mixed valence state.

Finally, it should be noted that preliminary results on $La_{0.67}Sr_{0.33}MnO_3$ samples are in agreement with those obtained for $La_{0.67}Ca_{0.33}MnO_3$.

# CHAPTER 1
# INTRODUCTION

The manganite perovskites have been the recent focus of literary attention. With various dopants, in particular the series $R_{1-x}A_xMnO_3$ (where R is a rare earth element such as La, and A is a divalent alkali metal, such as Ca or Sr), the material undergoes a ferromagnetic metal-insulator transition.[1-2] These compounds are based on the $AMO_3$ cubic perovskite structure with the Mn *d*-electrons playing a key role in both transport and magnetic order. One feature of these materials is that their characteristics are strongly dependent on doping concentration, x, and temperature. For example, the undoped compound $LaMnO_3$ (x=0) is an antiferromagnetic insulator with $Mn^{3+}$ ions. The *d*-orbitals order, distorting the original cubic lattice into an orthorhombic structure. Doping these materials with a divalent ion introduces holes, producing $Mn^{4+}$ ions. With sufficient doping, the mixed $Mn^{3+}/Mn^{4+}$ valency introduced by the $La^{3+}/A^{2+}$ substitution transforms the system into a ferromagnetic metal at low temperatures. Over the entire doping range, the materials are spin disordered, paramagnetic insulators above a critical temperature, $T_c$. The spin-ordered states below this critical temperature vary with doping concentration. For $x > 0.5$ and $x < 0.16$ the compounds are insulators with a variety of magnetic order depending on the doping concentration. The only metallic phase is found with ferromagnetic order in the intermediate doping range of $0.16 < x < 0.5$. In this intermediate doping regime, a ferromagnetic-paramagnetic transition is observed at a

$T_c(x) \approx 200\text{-}260$ K for $La_{1-x}Ca_xMnO_3$ and ~ 100 K higher for $La_{1-x}Sr_xMnO_3$. The materials in this ferromagnetic doped regime have been found to show huge magnetoresistance in the vicinity of the magnetic ordering temperature. The largest magnetoresistance effect is seen for a nominal doping concentration of $x = 1/3$.

In this metallic regime, the basic electronic transport mechanism believed to describe these materials is the double exchange mechanism.[3-5] Double exchange occurs when the spins of the charge carriers are aligned to the local atomic spins via a strong on-site Hund's coupling. Transport occurs as holes moving from one Mn site to another through the $Mn^{4+}$-O-$Mn^{3+}$ bond without the charge carriers changing their spin orientation.[3] The strong Hund's coupling enhances the hopping of the electrons between Mn sites, promoting ferromagnetic order. However, the double exchange interaction is insufficient to account for the large magnetoresistance observed in the manganese compounds. It has been postulated that a strong electron-lattice coupling mediated by a Jahn-Teller distortion of the $Mn^{3+}O_6$ octahedron must also be present.[6-8] A Jahn-Teller distortion is a single-molecule effect, which occurs when it is energetically favorable for the lattice of ions to distort resulting in a lower energy, lower symmetry structure.

These manganite materials exhibit several interesting electronic, magnetic, and structural properties making these compounds fascinating from both a physics and technological point of view. Interest from a pure physics perspective results from the interdependence of the charge, spin, and lattice degrees of freedom. Their strong correlation gives rise to a variety of physical phenomena including a metal-insulator transition that is contiguous with magnetic order and structural transitions. Another interesting aspect of the lanthanum manganites is band structure's prediction that the carriers are completely spin polarized.[9] The main technological impetus for the present interest in these manganites stems from their possible use in several areas of technology, including spin-polarized electronics, magnetic data storage devices, and read/write heads for hard disk drives.

In this study, the standard probe technique of tunneling is used to study thin film samples of $La_{1-x}Ca_xMnO_3$ and $La_{1-x}Sr_xMnO_3$, where x is nominally 1/3. This doping concentration was focused on because it shows the largest magnetoresistance in the ferromagnetic doping regime. At $T = 0$, the tunnel conductance is proportional to the product of the density of states for the two electrodes,

$$\frac{dI}{dV} \propto N_1(E)N_2(E) \qquad (1.1)$$

In a plot of current vs. voltage in the case of a superconducting electrode, the gap in the superconducting density of states appears as a region of low conductance. Observation of this behavior below the critical temperature of the superconductor ensures the quality of the junctions. In this study, this technique is used with a well-characterized superconducting electrode to study the density of electronic states of $La_{0.67}Ca_{0.33}MnO_3$ and $La_{0.67}Sr_{0.33}MnO_3$ thin films as a function of temperature and biasing voltage.

# CHAPTER 2
# TUNNELING SPECTROSCOPY

Ever since Giaever's pioneering work in quantum mechanical tunneling through a barrier and his discovery of the energy gap of indium, lead, and tin by this method, tunneling has become an important technique in the study of conducting materials.[10] Described in this chapter are the basics of tunneling through an insulating barrier and the relationship between the tunneling results and the density of electronic states of the system.

## 2.1 Metal-Insulator-Metal Tunnel Junctions

Quantum mechanically, an electron has a finite probability of passing through a region with a potential energy larger than the energy of the electron. This effect is called tunneling. The probability of tunneling through a specific barrier depends on the shape of the barrier, including its height and width.

One of the simplest examples of tunneling is a metal-insulator-metal tunnel junction, usually referred to as a normal-insulator-normal (NIN) junction. Often these are fabricated by depositing one metal strip and then oxidizing it to make an insulating barrier. A second strip is then deposited crossing the first. This "cross-strip" junction is sketched in figure 2.1. Typical insulating barriers are approximately 1 - 2 nm thick. In practice, the thickness of the barrier is varied until the resistance of the junction is in a useable regime for data acquisition. Typical room temperature resistances of a tunnel junction are in the range of $1 - 10^5\ \Omega$.

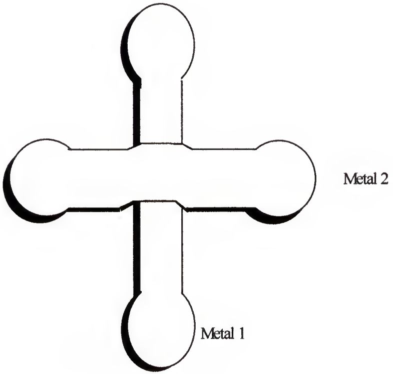

Figure 2.1: Cross-strip tunnel junction. The tunnel junction is the area of overlap between the two metal films.

The energy needed to remove an electron from the Fermi level of a material is its work function. Taking into account the electron affinity of the insulator simply lowers the effective barrier height but does not affect its overall shape. The two electrodes are not isolated metals when the barrier is thin enough for tunneling to occur. Therefore, in normal metals, electrons are transferred between the two electrodes until the two Fermi levels are at the same height. Dissimilar metals or electrodes form a slightly asymmetric potential barrier because each electrode has a different work function. Such a barrier has a slightly trapezoidal shape when its energy profile is sketched. However, for calculations such a barrier is approximated as rectangular. The barrier is further reduced by image forces; however, this is less than a 10% effect, which will be neglected for simplicity.

When a voltage, V, is applied between the metals, there is a displacement of the Fermi levels by an amount eV, with the positive side being lowered. An energy diagram for this situation is shown in figure 2.2. Electrons and holes in an energy range eV between the two shifted Fermi energies may elastically tunnel from occupied states on one side of the barrier to empty states on the other side. Of course, holes created on the right side of this diagram are continually filled by electrons flowing through the circuit due to the applied voltage.

There are two basic approaches for calculating the tunneling current, I(V), and conductance, $G(V) = \frac{dI}{dV}$, of tunnel junctions as a function of biasing voltage. The steady-state approach models a single wavefunction as extending smoothly across the entire tunneling structure. Standing wave behavior is modeled outside the barrier with an exponentially decaying wavefunction inside the barrier. A second approach uses a Hamiltonian picture with two separate standing waves, one on each side the barrier. Both wavefunctions exponentially decay in the barrier and beyond into the opposite electrode. Since both methods give the same result, only the steady-state approach will be presented here. Wolf's *Principles of Electron Tunneling Spectroscopy* presents both methods in detail.[11]

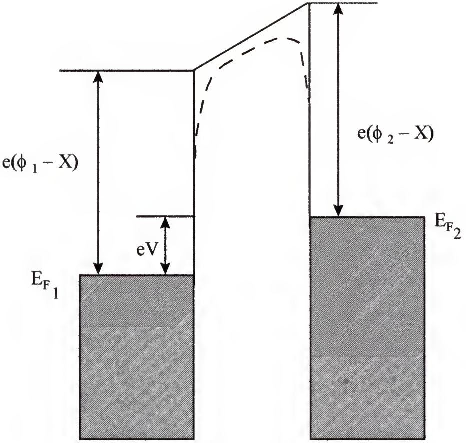

Figure 2.2: T = 0 energy diagram of a metal-insulator-metal junction with an applied biasing voltage, V. The curved broken line shows the effect of image forces on the barrier. X is the chemical potential of the insulator and $\phi_i$ is the work function of the metals. All states below the Fermi energy for each metal, $E_{Fi}$, are full as indicated by the hash marks. All states above the Fermi energy are empty.

### 2.1.1 T = 0 Steady-State Calculation

Several assumptions are made to simplify the calculations presented here. First, only electrons moving perpendicular to the barrier are considered in the following tunneling calculations. Second, it is assumed the tunneling process is elastic; therefore, the total energy of the system is conserved. Further, the transverse components of the wavefunction are also assumed conserved. These assumptions reduce the problem to one-dimension.

The tunneling current is the rate of transfer times the electric charge. Using Fermi's golden rule for the rate of transition from state 1 to state 2, the current flowing into side 2 can be written,

$$J_2 = \frac{2\pi e}{\hbar} \left| T_{12} \right|^2 N_2(E), \tag{2.1}$$

where $T_{12}$ is the tunneling matrix for transition from metal 1 to metal 2 and $N_2(E)$ is the density of states of metal 2 in the normal state at energy E. By the symmetry of the tunneling matrix element, $|T_{12}|^2 = |T_{21}|^2 = |T|^2$. To find the normal-normal tunneling current, $I_{nn}$, between states in the biasing range of 0 to eV, equation 2.1 is multiplied by the density of states of metal 1 and integrated over the biasing range,

$$I_{nn}(T=0) = \frac{2\pi A e}{\hbar} \int_0^{eV} | T |^2 N_2(E) N_1(E - eV) dE\,. \tag{2.2}$$

At $T = 0$, tunneling occurs in only one direction since there are no holes on the right side (metal 2) in line with electrons on the left side (metal 1). For a small biasing range, the tunneling matrix element and the density of states for both electrodes can be considered constant. Therefore, the integral reduces to eV. The current can be written as

$$I_{nn} = eG_n V, \tag{2.3}$$

where $G_n$ is the normal-insulator-normal tunneling conductance of the junction,

$$G_n = \frac{dI_{nn}}{dV} = \frac{2\pi Ae}{\hbar} |T|^2 N_2(0)N_1(0). \tag{2.4}$$

Hence, for NIN tunnel junctions, the current is linear with applied voltage and the conductance is directly proportional to the product of the density of states of the two electrodes.

### 2.1.2 $T \neq 0$ Steady-State Calculation

For $T \neq 0$, states above and below the Fermi surface are partially occupied. This smearing of the Fermi surface allows tunneling in either direction. The total tunneling current would then be the difference between the current to the right and the current to the left. Using the appropriate Fermi functions to describe the partially occupied states, the total current can be written as

$$I = |T|^2 \int_{-\infty}^{\infty} N_1(E-eV)N_2(E)f(E-eV)f(E)dE. \tag{2.5}$$

The tunneling matrix element, $|T|^2$, contains the effect of the barrier and is independent of the biasing voltage. The results of equations 2.3 and 2.4 are now approximate but still valid for low temperatures.

Simmons and Stratton extended the theory of tunneling to take into account effects such as temperature and high biasing voltage.[11] They both concluded that a correction term proportional to $V^3$ is needed in the basic linear dependence of the current with applied voltage. Therefore, for symmetric barriers, the conductance is found to be parabolic and symmetric about V = 0. An asymmetric parabola with a small offset (< 50 mV) from zero voltage can be reasonably described by a trapezoidal or asymmetric potential barrier.[12]

## 2.2 Metal-Insulator-Superconductor Tunneling

For the case of a superconducting electrode, a modification to the tunneling current and conductance is necessary to take into account the density of states of the superconductor, particularly the superconducting gap, Δ. Figure 2.3 shows a superconductor-insulator-normal metal (SIN) tunnel junction at T = 0. The hash marks indicate full electron states or empty hole states. No states can exist in the gap region at zero temperature.

At T = 0, no current can flow until eV = Δ, where Δ is the energy gap of the superconductor. At finite temperatures, there is a small current flow even at low voltages, because the electrons in the superconductor can be thermally excited across the energy gap occupying previously empty states. The following calculation is based on the simple BCS model. To calculate the tunneling current and conductance for the case of a superconducting electrode, $N_1(E)$ in equation 2.2 must be replaced by

$$N_s(E) = \begin{cases} \dfrac{N_n(E)E}{(E^2 - \Delta^2)^{1/2}} & |E| \geq \Delta \\ \\ 0 & |E| < \Delta. \end{cases} \tag{2.6}$$

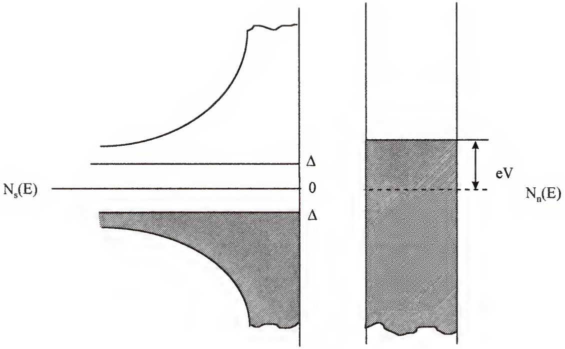

Figure 2.3: T = 0 energy diagram for a metal-insulator-superconductor tunnel junction with applied voltage, V. The hash marks represent full states. No states can exist in the superconducting gap region, Δ.

The current then becomes

$$I_{sn} = \frac{2\pi e A}{\hbar} \int_{\Delta}^{eV} |T|^2 \, N_n(E - eV) \frac{N_n(E)E}{(E^2 - \Delta^2)^{1/2}} dE \,. \tag{2.7}$$

Again, assuming a constant density of states and tunneling matrix element in the biasing range, the current reduces to

$$I_{sn} = \begin{cases} G_n((eV)^2 - \Delta^2)^{1/2} & eV \geq \Delta \\ & , \\ 0 & eV < \Delta \end{cases} \tag{2.8}$$

where $G_n$ is the same normal tunneling conductance found for the NIN tunnel junction (equation 2.4). In a plot of current vs. voltage for a SIN junction, the gap in the superconducting density of states appears as a region of low conductance (see figure 2.4). Observation of this behavior below the critical temperature of the superconductor ensures the quality of the tunnel junction.

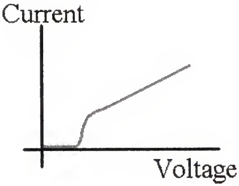

Figure 2.4: Sketch of a current vs. voltage plot for a superconducting electrode at T = 0. The region of low conductance corresponds to the energy gap of the superconductor.

The normalized superconducting tunneling conductance calculated from the current in equation 2.8 is

$$\frac{G_s(V)}{G_n} = \frac{dI_{sn}/dV}{G_n} = \begin{cases} \dfrac{|\mathrm{eV}|}{((\mathrm{eV})^2 - \Delta^2)^{1/2}} & eV > \Delta \\ & \\ 0 & eV < \Delta \end{cases} . \qquad (2.9)$$

These results are good approximations for $\mathrm{T} << \frac{\mathrm{T_C}}{2}$, where $\mathrm{T_c}$ is the critical temperature of the superconducting electrode. In this simple BCS model, Δ is taken as real and constant. However, in the strong-coupling theory of superconductors, Δ becomes complex and energy dependent; therefore, deviations from this theory are expected for strongly coupled superconductors such as Pb and Hg.

## 2.3 Schottky Barrier Effects

A standard assumption made in the preceding sections was that the insulating barrier's energy dependence could be approximated as rectangular. However, another type of barrier is prevalent in tunneling. A Schottky barrier has an electrostatic potential energy varying quadratically with distance as seen in figure 2.5. The main instance of Schottky barriers occurs for heavily doped semiconductor samples in direct contact with a metal electrode.

In this type of barrier, the thickness of the barrier potential is a function of the applied biasing voltage, as shown in figure 2.6. The application of a biasing voltage essentially raises the energy where tunneling occurs through the barrier. In figure 2.6,

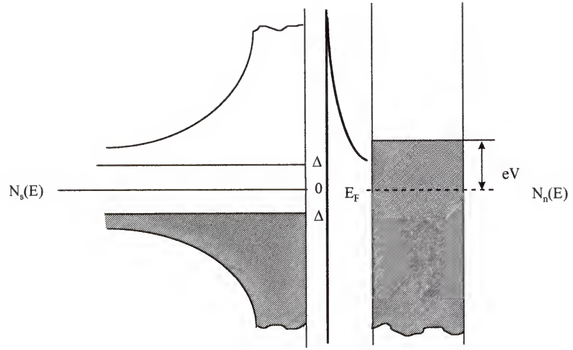

Figure 2.5: T = 0 energy diagram of a metal-insulator-superconductor tunnel junction with a Schottky barrier and applied voltage, V. The hash marks represent filled states. No states can exist in the superconducting gap region, Δ.

applied voltages $V_1$ and $V_2$ are shown, where $V_1 < V_2$. The conductance associated with $V_1$ will be larger than the conductance associated with $V_2$ based purely on the shape of the barrier. This leads to a background in the conductance data commensurate with the barrier shape.

Calculations by Conley, Duke, Mahan, and Tiemann (CMDT) use a parabolic barrier potential with bias-dependent width.[11] These calculations predict an exponentially dependent conductance with biasing voltage and a minimum at a bias energy equal to the Fermi energy. Therefore, low-bias data will appear linear instead of parabolic as expected for nearly rectangular barriers. The high-bias data ($V > 100mV$) will reveal the exponential dependence on applied voltage. Experimental evidence of this effect has been clearly seen with Pb on Ge:Sb samples.[11]

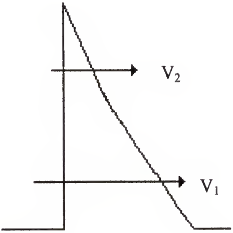

Figure 2.6: Sketch of a Schottky-like barrier with different applied voltages. $V_1 < V_2$.

The resistance of the tunnel junction is also affected by the height of the Schottky barrier. Higher resistance junctions correspond to higher barriers. This type of barrier is revealed in tunneling measurements by a background conductance that is bias dependent. As indicated in figure 2.7, lower resistance junctions have less change in the width of the barrier with applied bias. This corresponds to a smaller slope in the background conductance with applied voltage. In high resistance junctions, this background conductance will be more evident. A plot of tunneling conductance vs. voltage for several different resistance junctions would reveal an increasing slope with increasing junction resistance as sketched in figure 2.8.

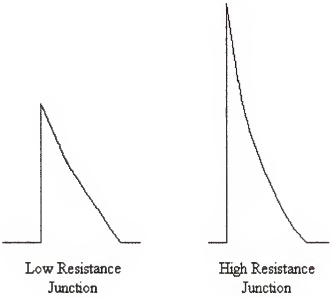

Figure 2.7: Sketch of a Schottky-like barrier profile for different resistance junctions.

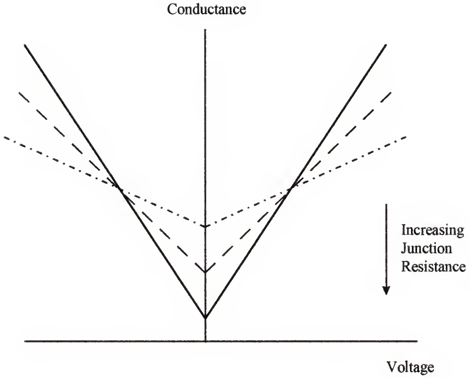

Figure 2.8: Sketch of a conductance vs. voltage plot for different resistance Schottky-like junctions. Higher resistance junctions reveal a steeper background slope.

# CHAPTER 3
# REVIEW OF $La_{1-x}(Ca, Sr)_xMnO_3$

A recent resurgence in the study of the rare earth manganites has been motivated by the remarkably large magnetoresistance properties exhibited by certain mixed valence materials. The electronic, magnetic, and structural properties of these materials make them of particular interest for use in new technologies. The primary focus of this chapter is to provide background on the physical properties of the rare earth manganites. The basic crystal structure and phase diagrams of these materials will be discussed, followed by the characteristics of these compounds. Some of the mechanisms believed to explain the manganites' unusual behavior are outlined.

## 3.1 Crystal Structure

The $R_{1-x}A_xMnO_3$ series is based on the cubic perovskite structure $AMnO_3$, where R represents a trivalent rare earth element such as La or Nd and A represents a divalent alkali element such as Ca, Sr, or Ba. As shown in figure 3.1, the R- or A-site ion is located at the body-centered position while the Mn ions occupy the corners and the oxygen ions are located in the middle of the unit cell edges. The oxygen octahedra centered on a Mn ion is also indicated, since it plays a key role in the transport properties of these materials.

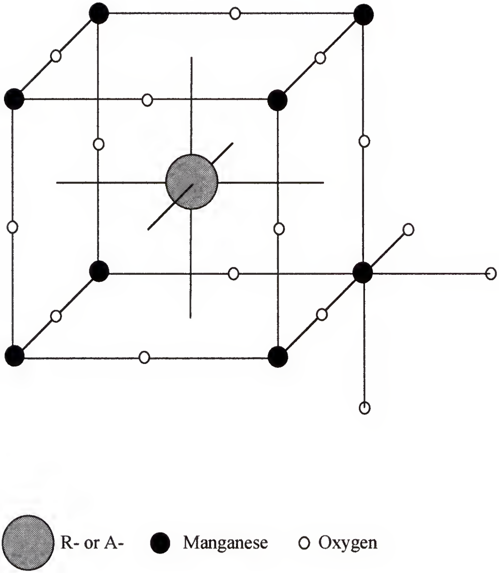

Figure 3.1: Sketch of the basic, undistorted perovskite structure. The Oxygen octahedron associated with a Manganese ion is shown in the lower right corner.

This ideal cubic structure is found for only optimal A-site ion radii. The deviation from the equilibrium bond lengths of a cubic structure can be expressed numerically by the Goldschmidt tolerance factor,

$$t(T,P) = \frac{r_D + r_O}{\sqrt{2}(r_T + r_D)}, \qquad (3.1)$$

where $r_D$ is the divalent ion radius, $r_T$ is the trivalent ion radius, and $r_O$ is the oxygen radius.[13] The tolerance factor is a function of temperature and pressure since the equilibrium bond lengths have different thermal compressions and expansions. A perfect cubic structure would have a tolerance factor, $t = 1$, while this ideal may occur over a limited range of temperature and pressure. For the materials under consideration, the A-site ion radius is smaller than ideal ($t < 1$), thus the crystal adapts by displacing the oxygen ions.

The displacement of the oxygen bends the $Mn^{4+}$-O-$Mn^{3+}$ bond angle from 180° to $(180° - \phi)$. Lowering the tolerance factor increases the distortion of the crystal and thus increases the $Mn^{4+}$-O-$Mn^{3+}$ bond angle deviation from 180°. The regularity of the oxygen distortion depends on the doping concentration of the material. For the undoped compound, $LaMnO_3$, there is a single size or type of A-site ion, therefore, the oxygen displacements are ordered and regularly patterned. For doped materials, such as $La_{1-x}Ca_xMnO_3$, different types or sizes of A-site ions are randomly distributed throughout the material resulting in randomly occurring oxygen displacements. In the manganites, the oxygen octahedra are not only tilted but elongated as well, forming an orthorhombic structure.

This structural distortion along with the intrinsic magnetic moment of Mn plays an important role in the transport properties of the manganite system. The important electrons for transport are the Mn *d*-electrons. In an ideal perovskite, the five Mn 3*d*-orbitals are split by the crystal field into a low lying $t_{2g}$ triplet and a higher energy $e_g$ doublet. The on-site Hund's rule exchange is large enough that the *d*-orbitals can be occupied by at most one electron. Jonker and van Santen pointed out that the substitution of divalent cations in the parent compound causes an equal number of $Mn^{3+}$ ions to change to $Mn^{4+}$.[14] Consequently, with doping concentration, x, there are (4-x) Mn *d*-electrons. Three occupy the $t_{2g}$ levels providing a strongly localized, electrically inert $S = 3/2$ core spin. The remaining (1-x) electrons occupy the $e_g$ level with spin oriented parallel to the core spin, again due to a strong on-site Hund's exchange coupling.

## 3.2 Phase Diagram

The phase diagram of $La_{1-x}Ca_xMnO_3$ reveals a number of electronic and magnetic phases in the material depending on the doping concentration and the temperature.[15-16] For example, the undoped compound $LaMnO_3$ (x=0) is an antiferromagnetic insulator with $Mn^{3+}$ ions. Replacing a trivalent rare earth site, for example $La^{3+}$, with a divalent ion, such as $Ca^{2+}$ or $Sr^{2+}$, introduces holes into the system causing a corresponding number of $Mn^{3+}$ ions to become $Mn^{4+}$ ions. This hole doping introduces free charge carriers (holes), increasing the conductivity of the material.

Over the entire doping range, the materials are spin disordered, paramagnetic insulators above a critical temperature, $T_c$. Varying the dopant type and concentration affects the critical temperature and the spin-ordered state below the critical temperature.

For example, Ca-concentrations below approximately 16%, and at or above 50%, exhibit insulating phases with various states of magnetic ordering at all temperatures; however, no metallic transition occurs. The only metallic phase is found with ferromagnetic order for the intermediate doping range of approximately $0.16 < x < 0.5$. All samples in this range exhibit the colossal magnetoresistance effect at the combined metal-insulator and paramagnetic-ferromagnetic phase boundary. This effect is one of the main properties of interest in these materials and will be discussed further in a subsequent section.

$La_{1-x}Sr_xMnO_3$ has a similar phase diagram to $La_{1-x}Ca_xMnO_3$ for doping concentrations between 20% and 50%.[17] The differences between these two cases are mainly due to the size difference between the Ca and Sr ions. $La^{3+}$ and $Ca^{2+}$ have very similar ionic sizes, 1.17 Å and 1.14 Å respectively,[18] leading to the expectation of the smallest structural changes compared to the parent compound, $LaMnO_3$. However, $Sr^{2+}$, with an ionic radius of 1.32 Å, has a more marked difference in the ionic size[18] compared to $La^{3+}$, forcing more structural changes compared to the parent compound. The most noticeable difference between Ca- and Sr-doped compounds is the critical temperature, $T_c$. Sr-doped materials exhibit a $T_c$ nearly 100 K higher than their Ca counterparts. The high temperature ($T > T_c$) behavior also differs slightly between the two doping types as will be discussed later.

The largest CMR effect is seen in the 33% doped materials, and for this reason research has centered on $x = 1/3$ compounds. The following sections concentrate on the physical properties and descriptions of $La_{1-x}Ca_xMnO_3$ in the ferromagnetic regime. The analysis can be extended to $La_{1-x}Sr_xMnO_3$ in the same concentration regime.

### 3.3 Colossal Magnetoresistance

Magnetoresistance (MR) is the effect of an externally applied magnetic field on a material's resistance. It is often defined as

$$MR = \frac{\rho(H=0) - \rho(H)}{\rho(H=0)} * 100\% . \tag{3.2}$$

Typical magnetoresistive behavior is only on the order of a few percent. The "Giant Magnetoresistance" (GMR) effect is found in multilayer thin film samples and granular mixtures that consist of alternating magnetic and non-magnetic materials. Such samples can have a larger magnetoresistive behavior, as high as approximately 20%. The largest percentage change in the magnetoresistance has been termed "Colossal Magnetoresistance" (CMR). Compounds exhibiting CMR characteristics include, but are not limited to, the manganite perovskites, the pyrochlores, and the spinels. In the manganites, a huge drop in magnetoresistance at $T_c$ results from a paramagnetic to ferromagnetic phase transition. The colossal magnetoresistance near $T_c$ can be nearly 100% as seen in some thin films of $La_{1-x}Ca_xMnO_3$.[19]

The strong temperature dependence of the resistivity in these CMR materials is demonstrated in figure 3.2 for a $La_{0.67}Sr_{0.33}MnO_3$ thin film. This CMR behavior is qualitatively the same for various dopant types and doping concentrations between $x = 0.20$ and $x = 0.45$. At high temperatures ($T > T_c$), $La_{1-x}Ca_xMnO_3$ displays semiconducting behavior ($\frac{d\rho}{dT} < 0$) and an activated resistivity ($\rho \sim \exp[(a/T)^{1/4}]$).[15] For Sr- or Ba- doped samples the high temperature behavior is semiconducting but the resistivity falls off nearly linearly with increasing temperature. For all dopant materials on cooling, the resistivity peaks at the Curie temperature, followed by sharp drop where the material enters a metallic phase ( $\frac{d\rho}{dT} > 0$ ). When an external magnetic field is applied, a magnetization is induced. This induced magnetization raises the temperature at which the paramagnetic to ferromagnetic transition occurs. The essential point is that the resistivity is a function of magnetization, whether the magnetization is produced with an external field, or by lowering the temperature. This metal-insulator transition is accompanied by the onset of spontaneous magnetization as demonstrated by the magnetization data in figure 3.3. Thus, the Curie temperature separates a high-temperature paramagnetic phase from a low-temperature ferromagnetic phase.

The mechanisms describing the correlation between the metal-insulator transition and the ferromagnetic-paramagnetic transition, which can account for the large magnetoresistance behavior seen in the ferromagnetically doped manganites, have been of extreme interest in recent years.

### 3.4 Double Exchange

Basic magnetic interactions between magnetic ions in a material typically include direct exchange and superexchange. Direct exchange occurs when the magnetic ions of a material interact because their charge distributions overlap, but this direct Coulomb interaction between the Mn *d*-electrons of two ions is not important in the manganites because the intervening oxygen ions preclude a direct overlap. Superexchange occurs

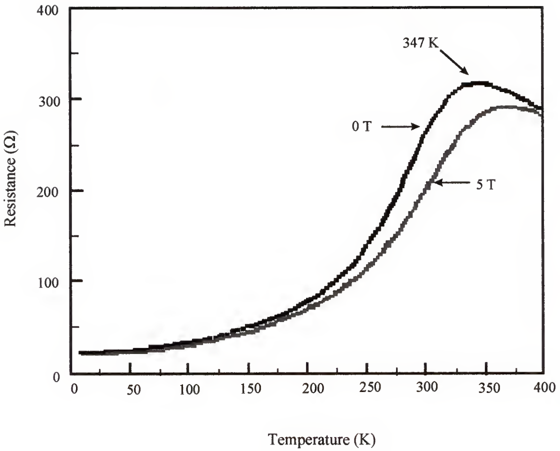

Figure 3.2: A typical resistivity vs. temperature data set from a $La_{0.67}Sr_{0.33}MnO_3$ thin film used in this study. A magnetic field of zero and 5 T was applied. The peak in the resistivity at zero field occurs at ~ 347 K, as indicated.
Data provided by Xiong (personal communication).

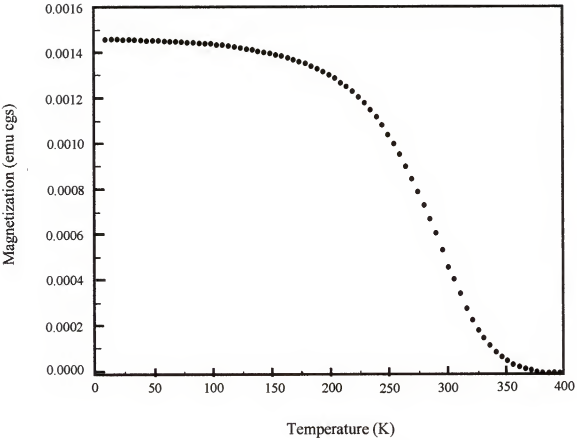

Figure 3.3: Magnetization vs. temperature graph taken at 0.1 T on the same film as shown in figure 3.2. Data provided by Xiong (personal communication).

when two magnetic ions with no charge distribution overlap are separated by a nonmagnetic ion such as oxygen. When the charge distributions of the magnetic ions overlap in the same neighboring nonmagnetic ion, a magnetic exchange interaction can occur. The interaction is then mediated by the electrons of the nonmagnetic neighbor. This virtual charge transfer rate is dependent on the angle between the spins of the magnetic ions, θ, by cosθ.[13]

The basic mechanism believed to link the electronic to the magnetic transition observed in the manganites was first proposed by Zener in 1951.[3] His "double exchange" interaction describes the real transfer of an electron from one $Mn^{3+}$ ion to a neighboring $O^{2-}$, with the simultaneous transfer of an electron from this $O^{2-}$ ion to a neighboring $Mn^{4+}$. A strong on-site Hund's coupling aligns the spins of the charge carriers to the local ionic spins. Since there is no mechanism for the carriers to change their spin orientation when moving, the neighboring sites must have parallel spins or the hopping rate is impeded. As the temperature is decreased, it then becomes energetically favorable for the Mn ions to align their spins ferromagnetically. The hopping electrons promote ferromagnetic order by preserving their spin direction, and the ferromagnetic alignment then results in a decrease in the resistivity. Anderson and Hasegawa showed that the transfer integral for electrons hoping through the $O^{2-}$ bond is dependent on the angle between the neighboring Mn moments, θ, by $\cos\frac{\theta}{2}$.[2] When the spins are antiferromagnetically aligned the transfer integral is zero.[4-5]

The double exchange interaction accounts for the low-temperature metallic behavior of the ferromagnetic manganites. However, as pointed out by Millis et al., the double exchange mechanism is insufficient to account for the magnitude of the resistance change observed in these compounds.[6-7] Millis et al. and Röder et al.[8] proposed that, in addition to a double exchange interaction, a strong electron-phonon interaction mediated by a Jahn-Teller distortion must be taken into account.

### 3.5 Jahn-Teller Distortion

As discussed earlier, it is not unusual for the oxygen octahedra to tilt in perovskite materials. However, in the manganites the magnitude and elongation of the oxygen octahedra indicates a Jahn-Teller distortion.[20] The Jahn-Teller distortion is a volume-conserving process where some Mn-O bonds elongate while others contract, lowering the energy and symmetry of the crystal. By looking at the energy diagram of the $Mn^{3+}$ ion, figure 3.4a, the effect of a Jahn-Teller distortion is clear.

The left side of figure 3.4a represents the undistorted lattice as described in section 3.1. It shows the low-lying $t_{2g}$ levels occupied by three electrons of parallel spin, forming the core spin. In this example, the core spin is indicated by the arrow in the upward direction. A large gap of 2 - 4 eV separates the $t_{2g}$ levels from the higher energy $e_g$ doublet. If the $e_g$ level is singly occupied, a Jahn-Teller distortion of the surrounding oxygen octahedra would split the $e_g$ doublet by an energy $E_{JT}$, removing the double degeneracy of the $e_g$ orbital. By perturbation theory, the energy of the system would be lowered but the strong Hund's coupling for the $e_g$ electron would maintain a spin parallel to that of the core electrons, as indicated on the right side of figure 3.4a.

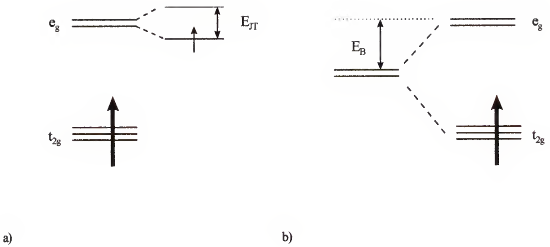

Figure 3.4: Energy diagram of the *d*-electrons for the Mn ion. a) The left side is the undistorted lattice. The right side indicates the effect of a Jahn-Teller distortion if the $e_g$ level is singly occupied. b) If the $e_g$ level is unoccupied, a breathing distortion may occur indicated by the left side with the undistorted lattice shown on the right side.

Another type of distortion is possible in the manganites when the $e_g$ level is unoccupied. A "breathing" distortion can occur, which lowers the energy of the unoccupied doublet by $E_B$ (figure 3.4b). The Mn-O bonds all lengthen or contract in a "breathing" distortion. Unlike in a Jahn-Teller distortion, volume is not conserved in a breathing distortion.

These distortions are driven by an energy gain, which depends on the valence of the center Mn ion. The oxygen octahedron will only Jahn-Teller distort around $Mn^{3+}$ ions because for the $Mn^{4+}$ ions the $e_g$ level is unoccupied. For the parent $LaMnO_3$ compound, the bond lengths will alternate from one Mn-site to another throughout the sample. The long-range order and coherent bond-length changes can be determined by conventional x-ray or neutron Bragg diffraction. A large (~10%) average bond length change has been seen for $LaMnO_3$ indicating a very strong Jahn-Teller distortion.[16] As the doping concentration, x, is increased, this structural distortion decreases because the $Mn^{4+}$ ions do not participate in a Jahn-Teller distortion. Still, the Mn-O bond length does change for the doped samples until the sample is fully-doped $CaMnO_3$. No Jahn-Teller distortion occurs for $CaMnO_3$ samples because there are only $Mn^{4+}$ ions; hence, the $e_g$ level is unoccupied.

### 3.6 Electron-Lattice Coupling

Two types of electron-lattice couplings have been discussed. One type involves the effect of the static crystal structure on electron hopping, depicted by the tolerance factor (section 3.1). The second type of electron-lattice coupling is a conventional dynamic effect that takes the form of a Jahn-Teller distortion or a "breathing" distortion (section 3.5). If the electron-phonon coupling is strong enough, the localization of carriers is possible. The presence of an electron in a given Mn orbital causes a local lattice distortion, which in turn produces a potential minimum. This potential minimum tends to trap the electron in that orbital. When the coupling is strong enough, as in some members of the manganite system, a self-trapped state can form. The local lattice distortion where the electron is trapped is called a polaron.

The energy gain of the localization of an electron due to polaron formation competes with the kinetic energy gain due to the delocalizing tendency of electron hybridization as favored by the double exchange interaction. This competing balance is very sensitive to the extrinsic temperature and applied magnetic field, as well as the intrinsic strength of the electron-phonon coupling and the doping (carrier density) of the material. In the $x \sim 1/3$ materials above $T_c$, the electron-phonon interaction is strong enough to localize the electrons, forming polarons. As the temperature is decreased through $T_c$, the system's growing ferromagnetic order shifts the balance so that the delocalization wins over the polaronic lattice distortions. The transition at $T_c$ is first-order, where the change is from small-polaron conduction in the paramagnetic phase to double-exchange interactions in the ferromagnetic phase.

### 3.7 Band Structure

The double exchange mechanism describes the ground state of the ferromagnetically doped manganites as half-metallic. Half-metallic implies one spin direction is metallic in character while the other is insulating. In other words, the carriers are 100 % spin-polarized. Focusing on the ferromagnetic manganites, the principal descriptions for this double exchange system above the ground state are given by Kubo and Ohata[21] and Furukawa.[22]

In Kubo and Ohata's description of the problem, the holes are assumed to couple antiparallel to the local spins. In the ferromagnetic state, all the local spins align. Only the spins antiparallel to this alignment can move to form a band. Therefore, the carriers are 100% spin polarized and the system has a half-metallic ground state. As the system disorders, for example by increasing the temperature, the spins antiparallel to the core spin are a combination of majority and minority carriers. This implies that the minority spin band is no longer empty even though the local moments retain their value.

Furukawa's treatment of this problem demonstrates that both the majority and minority spin states are split in the paramagnetic regime. As the system is magnetized, by reducing the temperature or applying a magnetic field, the spectral weight of the majority spin band must increase. Therefore, the spectral weight of the minority spin band decreases. This decrease continues until the ground state is reached where the minority spin band is empty.

More recent band structure calculations predict that a nearly half-metallic ground state exists in the ferromagnetic manganites.[23] Calculations show that the minority spin band does not collapse at low temperatures as expected for a true half-metallic material. Instead, the minority spin states are seen to exist even at T = 0. However, as a spin gap opens at low temperature, the minority carrier will be localized as polarons below the mobility edge. Therefore, at low-temperatures these materials will have half-metallic characteristics, including spin-polarized conduction.

# CHAPTER 4
# REVIEW OF EXPERIMENTAL EVIDENCE

Extensive experimental evidence exists that is consistent with the mechanisms described in chapter 3 for $La_{1-x}Ca_xMnO_3$ and $La_{1-x}Sr_xMnO_3$ polycrystalline and thin film samples. In the present chapter, results for the ferromagnetic samples that support the model of double exchange with strong electron-phonon interactions and polarons will be highlighted. Furthermore, previous tunneling studies on the manganites will be reviewed.

## 4.1 Transport and Thermodynamic Studies

Resistivity measurements show a distinct metal-insulator transition at $T_{MI}$. As mentioned previously in chapter 3, one of the unique properties of the manganites is that this metal-insulator transition occurs at approximately the same temperature, $T_c$, as an electronic and structural transition. Studies have been performed at high temperatures ($T > T_c$) as well as low temperatures ($T < T_c$) to better understand the transport mechanisms of these materials.

### 4.1.1 Low Temperature Resistivity

Based on a calculation of electron-magnon scattering in a double exchange system, Kubo and Ohata predicted the temperature dependence of the resistivity to have a $T^{4.5}$ dependence due to magnon scattering.[21] Schiffer et al. found for ferromagnetic $La_{1-x}Ca_xMnO_3$ ($0.2 < x < 0.45$) samples a resistivity that did have the predicted $T^{4.5}$ dependence, if an additional $T^2$ term was also taken into account.[15] The authors interpreted the $T^2$ term as representing electron-electron scattering. However, they point out that the low Debye temperature, $\theta_D \sim 500$ K, in these materials indicates that electron-phonon scattering should also be an important cause of resistivity. These results indicate a combination of electron-electron, electron-magnon, and electron-phonon scattering are significant in this system.

### 4.1.2 High Temperature Resistivity and Thermopower

From the resistivity data shown in figure 3.5, a negative magnetoresistance for $T > T_c$ is evident. The resistance in this temperature regime can be further described as thermally activated since the data can be fit with reasonable accuracy to an exponential of the form $\rho \approx \exp(\frac{E_\rho}{k_B T})$, where $E_\rho$ is the activation energy from the resistivity.

Studies show that the manganites possess a thermally activated thermopower, S(T), as well as a thermally activated resistance.[24-25] The high temperature thermopower also behaves as expected for a semiconductor, $S(T) \approx \frac{E_S}{k_B T}$, where $E_S$ is the activation energy of the thermopower. Any difference in these activation energies is directly proportional to the polaron formation energy. Experimental work shows that the activation energies differ by an order-of-magnitude, suggesting that small polarons exist above $T_c$.

### 4.1.3 Specific Heat

Specific heat, C(T), measurements of the perovskite manganites, $La_{1-x}Sr_xMnO_3$, have been measured as a function of doping concentration, $0 < x < 0.3$.[26] A term in the specific heat, $C \sim T^2$, is found in $LaMnO_3$ that is attributable to spin excitations. Samples of $x = 0$ and $x = 0.1$ doping show no linear term, $\gamma$, in temperature, which means the electronic component of the specific heat is negligible as expected for these insulating systems. For a metal

$$\gamma = \frac{1}{3}\pi^2 k^2 N(E_F), \tag{4.1}$$

where $N(E_F)$ is the density of states at the Fermi surface,[27] and a negligibly small $\gamma$ then implies a small $N(E_F)$, which is a description of an insulator. On the other hand, the ferromagnetic samples $x = 0.2$ and $x = 0.3$ have the expected specific heat term $C \sim T^{3/2}$ due to ferromagnetic spin waves, as well as the linear electronic contribution. These results are consistent with the metallic behavior indicated by the resistance measurements.

### 4.1.4 Thermal Conductivity

Thermal conductivity, $\kappa$, measurements as a function of temperature and magnetic field also show lattice effects which can be interpreted by a polaron transport model.[28] The electronic contribution to the thermal conductivity in the paramagnetic region was found to be negligible, consistent with adiabatic small polarons. Thermal conductivity results reveal a dominant lattice contribution governed by static rather than dynamic distortions of the oxygen octahedra. The double exchange plus strong electron-phonon model yields the appropriate framework for the local physics of the lattice distortion and charge mobility effects seen in thermal conductivity experiments.

### 4.1.5 Isotope Effect

The general importance of polarons due to a Jahn-Teller distortion of the crystal structure has also been demonstrated by the large isotope effect on $T_c$. Replacing $^{16}O$ by $^{18}O$ in $La_{1-x}Ca_xMnO_{3+\delta}$ results in a reduction of $T_c$ by as much as 20 K or 10%.[29] This effect can be understood by the motion of oxygen ions when the Jahn-Teller distortion occurs and indicates a strong spin-lattice coupling. The universal field dependence of the lattice parameters shown in neutron scattering data also shows that the spin ordering is strongly coupled to the lattice.[30] The neutron scattering data also clearly demonstrate a variation of the lattice parameters as a function of magnetic field. Above the Curie temperature, a decrease in the tilting angles of the oxygen octahedra with decreasing temperature is observed. This is followed by a sharp change at $T_c$, which remains constant for lower temperatures.

### 4.1.6 Optical/Raman Spectroscopy

Raman studies on manganite materials in the ferromagnetic regime reveal a diffuse scattering response in the paramagnetic phase that reduces to a flat scattering response as the temperature is lowered through $T_c$.[31] These authors interpret their scattering results as the transport being dominated by small polarons at high temperatures and large polarons below $T_c$. Furthermore, evidence for small polarons existing in the low temperature regime with the large polarons is observed.

Optical conductivity measurements on $La_{0.7}Ca_{0.3}MnO_3$, $La_{0.7}Sr_{0.3}MnO_3$, and $Nd_{0.7}Sr_{0.3}MnO_3$ also indicate the existence of a Jahn-Teller small polaron in the paramagnetic state of these materials.[32] The small polarons are also seen in the ferromagnetic state; however, they decrease in strength as the temperature decreases. The optical data presented agrees with models of the double exchange mechanism with the Jahn-Teller effect.

## 4.2 Structural Experiments

### 4.2.1 EXAFS

Evidence for the predicted existence of local lattice distortions includes extended x-ray absorption fine structure (EXAFS) data. EXAFS measurements study the local atomic structure around a central atom. Booth et al. measured the distortion of the Mn-O bond length distribution with temperature for various doping concentrations.[33] As discussed in chapter 2, $LaMnO_3$ has the largest Jahn-Teller distortion of the lattice while $CaMnO_3$ has no Jahn-Teller induced lattice distortion. For samples with intermediate doping, bond-length distortions above $T_c$ tend to plateau to a single value on the same order as seen for the distorted $LaMnO_3$ lattice. The distortion drops to a value typical of the undistorted $CaMnO_3$ as the temperature is lowered through $T_c$. These data clearly indicate the existence of lattice distortions at $T_c$. XAFS measurements preformed on $La_{0.67}Ca_{0.33}MnO_3$ also show a change in the Mn-O bond length distribution at $T_c$ consistent with small polaron related local Jahn-Teller distortions.[34]

### 4.2.2 Neutron Scattering

Lynn et al. performed neutron scattering measurements on polycrystalline $La_{0.67}Ca_{0.33}MnO_3$ samples to study their magnetic order, spin dynamics, and structural properties.[35-36] They observed that the magnetic system at low temperatures behaves as an ideal isotropic ferromagnet. The magnetic excitations were fit as conventional spin waves with the dispersion relationship

$$E = \Delta + D(T)q^2, \tag{4.2}$$

where $\Delta$ is the spin wave energy gap and D(T) is the spin stiffness coefficient. They found no spin wave energy gap within the resolution of the equipment (< 0.04 meV), indicating a soft ferromagnet. Unexpected results were seen for the $x = 1/3$ doping concentration as the temperature of the sample was increased toward $T_c$. A non-vanishing spin stiffness coefficient, $D(T_c) \sim \frac{1}{2}D(0)$, was observed as well as a quasielastic component to the fluctuation spectrum above 200 K which proceeded to become the dominant spectral weight at $T_c$. This behavior is atypical of isotropic ferromagnets and is only found in the $La_{1-x}Ca_xMnO_3$ materials when $x \approx 1/3$. With the application of an external magnetic field the central component of the fluctuation spectrum shifted into the spin wave component. Increasing the applied field increases the amount of shift. The authors suggest that the quasielastic component is associated with the localization of electrons and may be related to the formation of spin polarons in the system. This picture has been confirmed recently by measurements on single crystal samples, along with the direct observation of lattice polarons that form near and above $T_C$.[37]

### 4.2.3 Neutron Scattering Pair Density-Function Analysis

Pair-density-function (PDF) analysis represents the distribution of atom-atom distances or local structure of the system under study. Based on PDF analysis of neutron powder-diffraction data on $La_{1-x}Ca_xMnO_3$ samples, Billinge et al. observed a transition at $T_{MI}$ from a state with disordered bond lengths at high temperatures to a state with a uniform bond lengths at low temperatures.[38] The authors interpreted these results as a direct observation of conventional breathing type polarons in the insulating phase. No polaron formation was seen in the metallic phase of the material. Thus, their conclusion was that the polaron formation is unrelated to a Jahn-Teller distortion. Similar experiments and analysis on powder samples of $La_{1-x}Sr_xMnO_3$ led Louca et al. to conclude a direct relationship between polaron formation and the Jahn-Teller distortion.[39] Their results show a local Jahn-Teller distortion is present in the metallic phase of the material as well as the insulating phase. Clearly more work needs to be done to elucidate the origin of polaron formation in this material.

## 4.3 Previous Tunneling Experiments

Only a few tunneling studies have been carried out previously on the manganite materials, and these can be divided into two general categories, scanning tunneling measurements and trilayer tunnel junction experiments. Scanning tunneling spectroscopy measurements are taken with a Scanning Tunneling Microscope (STM). The data are taken during an STM scan of the sample by measuring the tunneling current as a function of sample bias voltage. Normalized conductance data are obtained either from the I-V measurements or by analog derivative measurements using a lock-in amplifier. One common artifact seen in scanning tunneling data arises from a Coulomb blockade effect and caution must be observed when interpreting tunneling spectra. Fortunately, the size of a Coulomb gap is highly dependent on temperature and tip-to-sample capacitance, and thus can be clearly identified.

Trilayer tunnel junctions are samples in the form of [(top electrode) manganite film]/[insulating barrier]/[(bottom electrode) manganite film]. The insulator usually deposited is $SrTiO_3$ because of its close lattice match to the manganite films. Current and dynamic resistance vs. voltage measurements can be directly obtained from these samples. One difficulty in this method is the fabrication of the tunneling structure, as a thin, defect-free artificial barrier can be difficult to manufacture. In both methods, the caliber of the tunnel junction is difficult to evaluate because no quality-dependent characterization exists for these junctions, in contrast to a planar tunnel junction which uses a well-characterized superconductor as an electrode. In the latter case, observing the superconducting characteristics below the superconducting critical temperature not only insures that tunneling is the dominant conduction mechanism, but also is an indication of the quality of the junction.

### 4.3.1 Scanning Tunneling Spectroscopy

Scanning tunneling spectroscopy has been performed on $La_{0.7}Ca_{0.3}MnO_3$ films and single crystals.[40-41] Results taken from film studies reveal pronounced peaks in the conductance at 77 K that are absent above the critical temperature, $T_c \sim 260$ K.[40] The authors interpret these results as direct evidence for half-metallic ferromagnetism, resulting from the combined effect of double-exchange and lattice distortion in the doped manganites. Reports on $La_{1-x}Ca_xMnO_3$ ferromagnetic single crystals and thin films as a function of temperature and applied magnetic field reveal a magnetic field dependence of the high-bias (V > 1 V) tunneling conductivity which decreases rapidly with increasing field up to 1 T.[41] The conductance continues to slowly decrease up to the experimental limit of 9 T with no observed saturation. The author concludes that the metal-insulator transition seen in these materials is due to percolation effects.

### 4.3.2 Trilayer Tunneling Spectroscopy

Tunneling conductance measurements taken at 4.2 K on $La_{0.67}Sr_{0.33}MnO_3$ trilayer structures reveal a parabolic conductance background as a function of biasing voltage consistent with tunneling.[42] Measurements were obtained of the magnetoresistance ratio, $\frac{R_{\max} - R_p}{R_p}$, where R is the maximum tunneling resistance and $R_p$ is the saturation resistance at fields where the moments of both electrodes are parallel. At 4.2 K, the largest MR ratio (~ 83%) is found at a few tens of Oersted. Using the relationship,

$$\frac{R_{\max} - R_p}{R_p} = \frac{2P^2}{1 - P^2} \tag{4.3}$$

where P is the spin polarization for the $La_{1-x}Sr_xMnO_3$ film, an experimental spin-polarization of ~ 0.54 is obtained. Further measurements of the magnetoresistance ratio show a large temperature dependence that becomes negligible with increasing temperature well below the $T_c$ of the material. Explanations of this temperature dependence include a non-ideal insulating barrier, a temperature dependent polarization, or enhanced electron-magnon scattering causing increased spin flipping with temperature.

These recent experimental measurements point to the fact that double exchange with strong electron-phonon interactions is consistent in explaining the behavior of the manganite systems. The data indicate that small polarons do exist above $T_c$ and do not completely disappear in the low temperature regime. To better characterize the physics behind the manganites, we have measured the density of electronic states of thin film manganite samples as a function of temperature and applied voltage for natural barrier tunnel junctions.

# CHAPTER 5
# FABRICATION

This chapter describes the fabrication techniques used to form the tunnel junctions investigated. Typical characterizations of the thin films, $La_{0.67}Ca_{0.33}MnO_3$ and $La_{0.67}Sr_{0.33}MnO_3$, used in this study are given, followed by a description for two different techniques used to form the tunneling barrier. The junctions were fabricated using Pb counterelectrodes. Both methods were found to produce high-quality junctions, which exhibited the expected phonon structure associated with the Pb electrode below its superconducting critical temperature.

## 5.1 Film Characterization

The thin films of $La_{0.67}Ca_{0.33}MnO_3$ and $La_{0.67}Sr_{0.33}MnO_3$ used in these measurements were grown and characterized by Xiong (personal communication). The films were deposited on $LaAlO_2$ (100) single-crystal substrates using a pulsed laser ablation system, with the film thickness varying from approximately 15 to 20 nm. The temperature dependence of the resistance of a typical $La_{0.67}Ca_{0.33}MnO_3$ film is shown in figure 5.1, with a $T_c \sim 247$ K as indicated. Characterizations of a typical $La_{0.67}Sr_{0.33}MnO_3$ film were previously shown in figures 3.2 and 3.3, with a $T_c \sim 347$ K. These values agree with previously reported $T_c$'s for similar thin films and are comparable to bulk values.[43] Figure 5.2 shows magnetization data as a function of temperature taken at 0.1 T. The

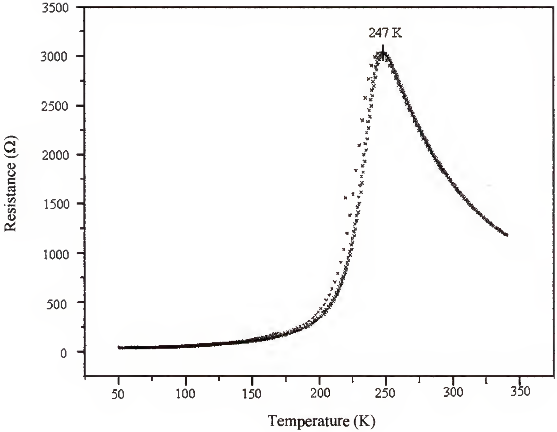

Figure 5.1: Typical $La_{0.67}Ca_{0.33}MnO_3$ resistance vs. temperature. The peak resistance occurs at ~ 247 K, as indicted. Data provided by Xiong (personal communication).

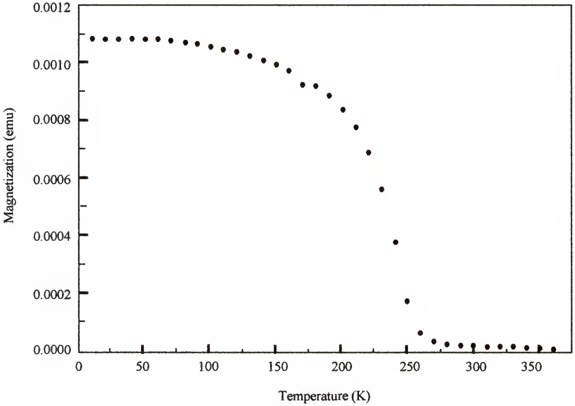

Figure 5.2: Magnetization vs. temperature taken at 0.1 T for the same $La_{0.67}Ca_{0.33}MnO_3$ film shown in figure 5.1. Notice that the onset temperature for this magnetization data is approximately the same as found for the resistivity data, ~ 247 K. Data provided by Xiong (personal communication).

sharpness of both the resistance peak and the onset of magnetization demonstrates the high quality of these films. Notice that the magnetic ordering at $T_C$ occurs at approximately the same temperature as the peak of the resistivity.

## 5.2 Tunnel Junction Preparation

The films characterized in the preceding section are chemically etched into a thin stripe and used as the lower electrode in a "cross-stripe" tunnel junction (figure 2.1). This is accomplished by masking off a thin strip of the manganite film, approximately 1 mm wide, in the center of a 5 $mm^2$ piece of the thin film. When possible, the stripe is formed in an area devoid of defects or formed parallel to any twinning of the substrate. It has been observed that junctions formed over a twined area have poor tunneling characteristics, possibly due to different phase contributions across the twinned boundaries. The sample is etched using equal-part solutions of phosphoric acid, hydrogen peroxide, and water. The mask is then removed, leaving the base electrode for tunnel junction fabrication. As expected, no change in the film characterization is observed due to this processing.

The experimental difficulty in making these tunnel junctions is the formation of a insulating barrier that is uniform, free from holes, and thin enough (~ 1 - 2 nm) to allow tunneling. Two different methods for forming an insulating barrier have been used in this study. Both methods have proven effective on other perovskites.[44-45]

### 5.2.1 Ion-milled Barrier

High-quality junctions are easier to form over smaller areas simply because there are fewer defects in the film and barrier. Using basic optical resist processing techniques, the sample is masked off except for a small area (~ 20μm$^2$) on the manganite film, where the junction will be formed. A slotted copper TEM grid is centered on the exposed area and attached perpendicular to the manganite stripe to delineate the Pb electrode, see figure 5.3. The slot in the copper grid needs to be at least twice as wide as the tunnel junction area to avoid sputtering any copper into the junction area during the ion-milling process.

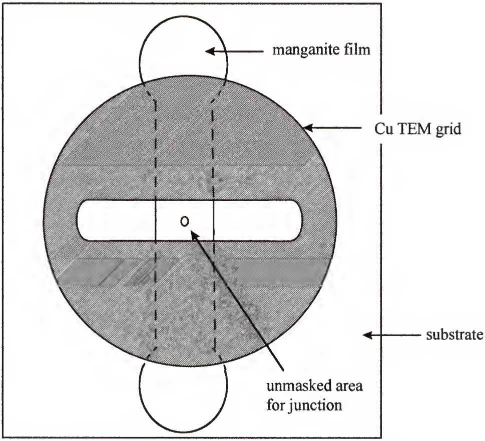

Figure 5.3: Sketch of the sample before the barrier and top electrode are formed.

The barrier and Pb electrode are formed in a high-vacuum deposition chamber. The deposition chamber employed is a diffusion-pumped, 8-inch diameter stainless-steel cylinder with a base pressure of $4.0 \times 10^{-7}$ Torr. It is equipped with a Kauffman ion mill, as well as several thermal evaporation sources. Research grade (99.995%) argon or xenon gas is employed with the ion mill at (uncompensated) ion-gauge pressures of approximately $1.0 \times 10^{-4}$ Torr.

Barrier formation is a two-step process involving the ion mill. In the first step, the sample is exposed to a 300 V beam for a duration of 1.5 minutes, which cleans and smoothes the exposed surface of the film. The second step forms the insulator. The final steady state resistance of the barrier is determined by adjusting the beam current or voltage of the ion mill or the time of exposure. Higher beam energies cause deeper damage into the film, increasing the resistance of the junction. The film is exposed to a beam of 100 V for 2 minutes, producing junctions with a typical room temperature resistance of $10^2 - 10^4\ \Omega$. Finally, a film of Pb (~ 0.5 μm thick) is thermally deposited across the junction to form the top electrode.

Initially, the junctions were fabricated using argon as the ionizing gas. However, the tunneling characteristics of the superconducting Pb electrode were not sharp or well defined. The expected phonon modes of the superconducting Pb electrode were smeared by leakage currents, indicating the tunnel junctions formed were of moderate quality. A lower beam voltage in the second stage of barrier formation improved the quality of the tunneling characteristics by reducing the depth of damage into the manganite film. However, a constant, reproducible beam could not easily be produced at low enough beam voltages for the high-quality junctions desired. Therefore, the argon gas was replaced with xenon in the milling process. The mass of the ionized gas determines the depth at which damage occurs in the film. By milling with xenon, a heavier atom, the damage is confined to a thinner layer of the film. Figures 5.4 and 5.5 clearly show that higher quality junctions are formed using xenon rather than argon as the ionizing gas. More data points in and near the gap region are needed for a better characterization of the junctions. However, several features indicate junctions formed using xenon gas are of higher quality than the ones formed using argon gas. Not only does the xenon junction show a sharper, more defined region of low conductance in the I-V characteristics, a larger, more distinct superconducting gap edge in the conductance data is clearly visible. The conductance data reveal the Pb phonon modes expected below the critical temperature, 7.2 K, of this superconducting electrode. Further, a low conductance is measured in the superconducting gap region of the xenon junction.

All these features indicate a high-quality junction. One method for quantifying the quality of the tunnel junction is to measure the resistance ratio,

$$\delta R = \frac{R_S(V=0)}{R_N}, \tag{5.1}$$

where $R_S$ is the resistance of the junction in the superconducting state and $R_N$ is the normal state resistance. For high-quality tunnel junctions, $\delta R > 100$; for an average tunnel junction, $\delta R \sim 40 - 50$. In figures 5.4 and 5.5, the argon junction has a $\delta R \sim 6$ while the xenon junction has a $\delta R \sim 40$.

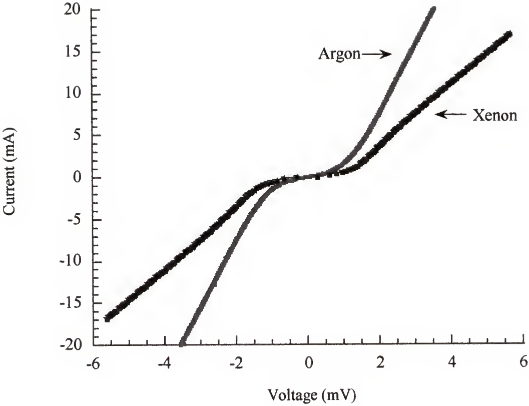

Figure 5.4: Current vs. voltage data at 2 K, comparing the ion-milled junctions using argon and xenon gas. The junction formed using the xenon gas shows a sharper, more defined superconducting structure for the Pb electrode.

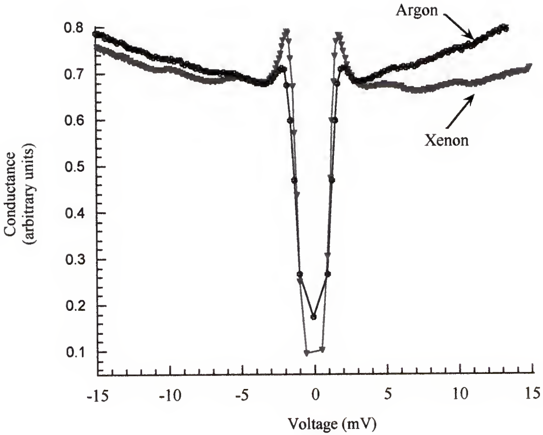

Figure 5.5: Conductance vs. voltage data at 2 K, comparing the ion-milled junctions using argon and xenon gas. The junction formed using the xenon gas shows a sharper, more defined superconducting structure for the Pb electrode. $\delta R_{xenon} \sim 40$. $\delta R_{argon} \sim 6$.

### 5.2.2 Chemically Formed Barrier

High-quality junctions were not achievable with the ion milling procedure if optical inspection using polarized light at a magnification of 1000 indicated that the films had rough surfaces. However, junctions of quality equal to the best ion-milled films could be obtained using a chemical means of fabricating the barrier. In this second method, the entire $La_{1-x}Ca_xMnO_3$ film is etched in a solution of 1 ml of bromine to 20 ml methanol for 10 minutes. The junction area is then defined by masking all but a small area the film with a fast drying glue; such as Duco cement. The Pb electrode is delineated by a Cu TEM slotted grid and thermally deposited as in the previous method.

Both ion-mill and chemical etch methods produce high-quality junctions with nearly identical conductance characteristics at all temperatures. Figure 5.6 compares the conductance data of a chemically created barrier junction to a xenon-milled junction. All the temperature data sets are essentially identical. This indicates that the results are independent of the method used to form the barrier.

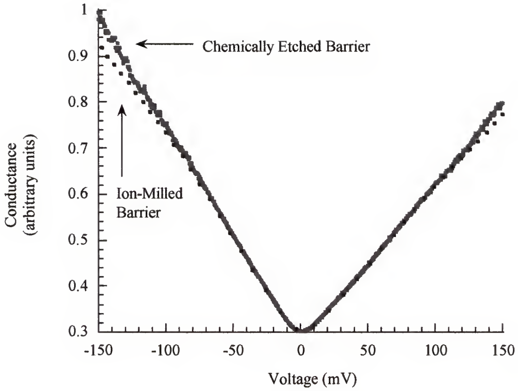

Figure 5.6: Unnormalized conductance vs. voltage characteristics at 43 K, comparing a chemically etched barrier and an ion-milled barrier using xenon gas.

# CHAPTER 6
# DATA ACQUISITION

## 6.1 Measurements

Measurements of current versus bias voltage and conductance versus bias voltage were taken for temperatures ranging from 2 K - 300 K. The circuit diagram for current measurements as a function of biasing voltage is shown in figure 6.1. In the diagram, $R_J$ is the resistance of the tunnel junction. The value of the dropping resistor, $R_d$, is changed to be typically one to two orders of magnitude larger than the junction resistance so that it will dominate the total circuit resistance. Therefore, any changes in the junction resistance will not significantly effect the current in the circuit, making this circuit essentially act as a constant current source. Data are taken on an XY plotter or by a computer running a LabView program. High-input-impedance, low-noise pre-amplifiers are used to measure the current and voltage. Using a standard four-terminal technique ensures the measured voltage does not include the voltage drops across the contacts or leads. Initially, a room temperature I-V curve is taken to ensure the sample has a reasonable resistance. The sample is then cooled well below the superconductor's critical temperature to reduce any smearing of the tunneling characteristics due to thermal excitations. A second I-V curve is taken to verify the quality of the tunnel junction.

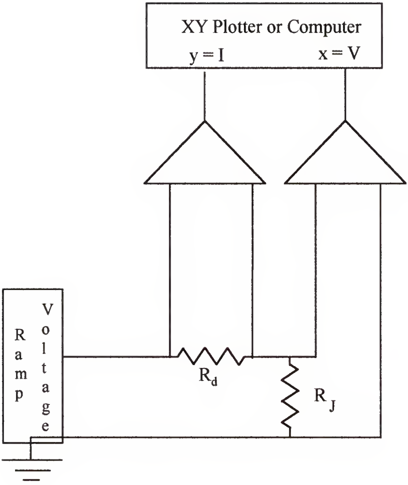

Figure 6.1: Diagram of the circuit used to measure the current as a function of voltage for a tunnel junction. $R_d > 10\ R_J$.

Measurements of the dynamic resistance, dV/dI, are obtained using the circuit shown in figure 6.2. These measurements require two current sources, one with a slow DC ramp and one with a constant amplitude AC modulation. The currents are routed through an operational amplifier adder circuit. The DC part of the signal determines the bias point, while the AC modulation is used to find the dynamic resistance. Again, $R_J$ is the resistance of the tunnel junction and a dropping resistor, $R_d > 10\ R_J$, is used to keep the current in the circuit essentially constant. The voltage across the junction consists of AC and DC components. The two signals are separated by splitting the signal lead and feeding one set capacitively into a pre-amplifier while the other set is fed directly into a pre-amplifier. The modulation voltage across the junction is measured using an analog lock-in amplifier and is proportional to the dynamic resistance of the junction, $dV/dI$. A typical excitation frequency of 270 Hz is generated and detected with the lock-in amplifier. The data are taken on an XY plotter or a computer running a LabView data acquisition program. It is then inverted to yield conductance ($dI/dV$) as a function of applied dc bias voltage, V. All data acquisition is preformed in a rf-shielded room using standard low-noise techniques. The computer is placed outside the rf-shielded room. A direct electrical link between the computer and the measurement apparatus is removed with the use of a fiber-optic link to drive and record the equipment inside the shielded room. The data sets to be presented were obtained as the sample slowly warmed up from 2 K unless otherwise noted. The temperature was held essentially constant, $\Delta T < 0.2$ K, for each data sweep.

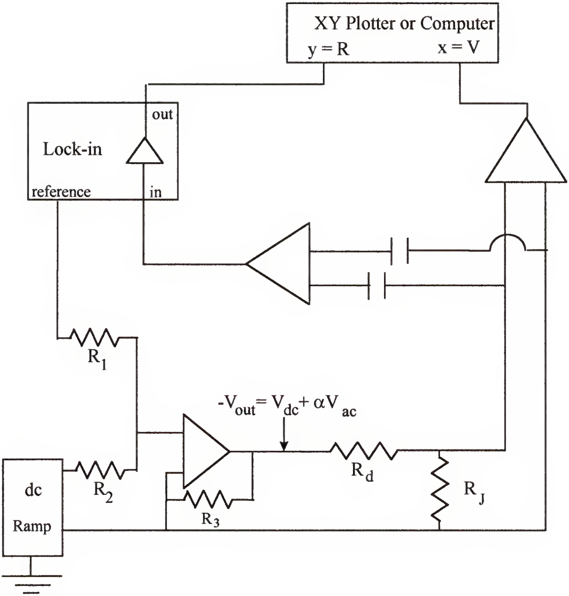

Figure 6.2: Diagram of the circuit used to measure the dynamic resistance, dV/dI, as a function of voltage for a tunnel junction. $R_d > 10\ R_J$ and $\alpha << 1$.

## 6.2 Junction Quality

In this study, planar tunnel junctions are fabricated using the manganites as the bottom electrode and the well-characterized superconductor, Pb, as the top electrode. It is important to characterize the Pb film well below its critical temperature of approximately 7.2 K to insure the quality of the tunnel junction. Because Pb is a strongly coupled superconductor, deviations from the BCS model, equations 2.8 and 2.9, are expected. Other than the region of low conductance expected for all isotropic superconductors with a gap, it is possible to observe inelastic coupling of phonons in the conductance spectra. The inelastic excitations cause approximately a 10% deviation in the conductance at characteristic energies. Therefore, observation of the transverse and longitudinal Pb acoustic phonon modes centered at voltages of ~7 mV and ~11 mV, respectively, indicates a junction of high-quality.

Typical current and conductance measurements as a function of biasing voltage are shown in figure 6.3 for a temperature of 2 K. Since $T << \frac{T_C}{2}$ here, thermal excitations are minimized, and consequently equations 2.8 and 2.9 are reasonable approximations. The region of low conductance associated with the superconducting gap of Pb is visible in the I-V data, figure 6.3a. The gap voltage, estimated from figure 6.3b, was found to be 1.30 mV, which agrees with a previously reported value of 1.36 mV.[46] The sharp superconducting gap edge, the negligibly small zero-bias conductance in the gap region, and a $\delta R \sim 80$ are all indications of a low leakage junction with no barrier-related inelastic processes.

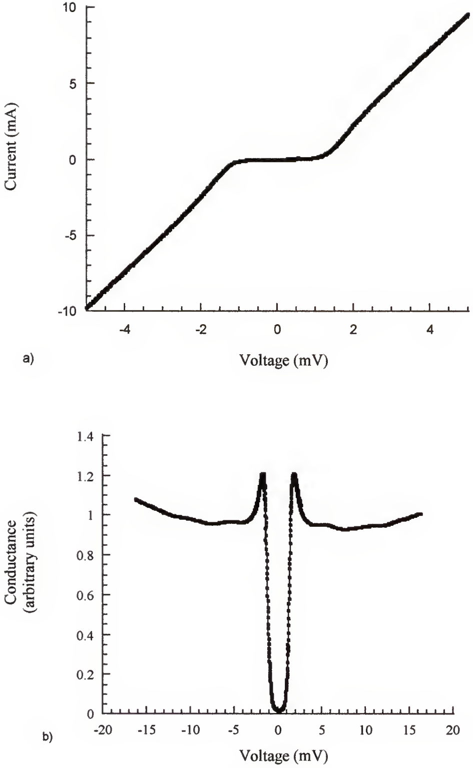

Figure 6.3: Tunneling data taken at 2 K. a) I-V characteristics show the region of low conductance associated with the superconducting gap of Pb. b) Normalized conductance vs. voltage data reveal a sharp gap edge and the Pb phonon modes.

As indicated in section 2.7, Schottky-like barriers have identifying characteristics such as a linear background tunneling conductance at low-bias and an exponentially dependent conductance background at high-bias. Several features of the tunneling conductance data for the manganite films indicate that a Schottky-like barrier exists in these junctions. First, at low-bias ($V < 100$ mV) a linear background is seen in the conductance spectrum. Second, as shown in figure 6.4, higher resistance junctions have steeper linear backgrounds with applied biasing voltage. In this graph, the zero-bias resistance has been shifted for clarity. Third, the conductance data for voltages greater than 100 mV can be fit to an exponential of the form $\exp[\frac{V}{E_\infty}]$ as indicated in figure 6.5. From the fit we obtain $E_\infty \sim 156$ mV. In the analysis of the conductance data, the Schottky-like barrier effect can be minimized by dividing out the low-bias linear background.

To compare these data with BCS theory, the linear background of the conductance data must be removed. Figure 6.6 plots this normalized conductance data for voltages between 0 and 15 mV. The predicted behavior described by the $T = 0$ BCS theory (chapter 2) is shown by the dashed line. A gap voltage of 1.30 mV measured from the conductance data was used in the fit. The Pb phonon modes are centered at approximately 7 mV and 11 mV, as expected.

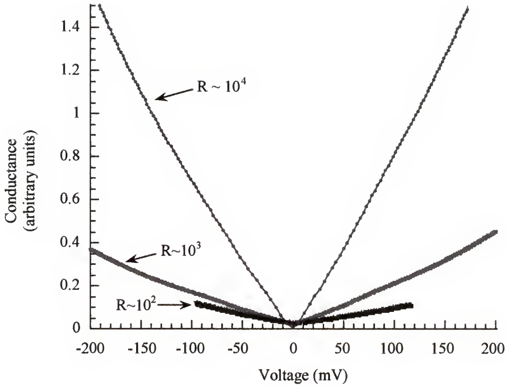

Figure 6.4: 10 K conductance vs. voltage measurements for different room-temperature-resistance junctions. Higher resistance junctions reveal a steeper background conductance, indicative of a Schottky-like barrier.

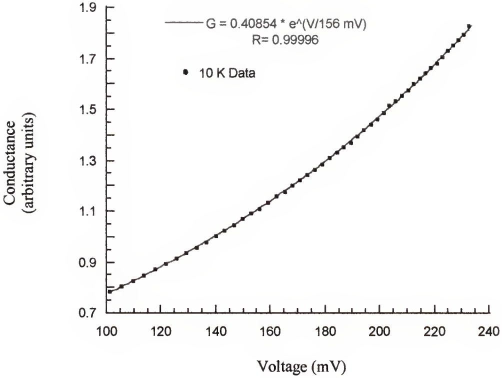

Figure 6.5: Conductance vs. voltage measurements at 10 K for voltages greater than 100 mV. The solid curve is an exponential fit to the data.

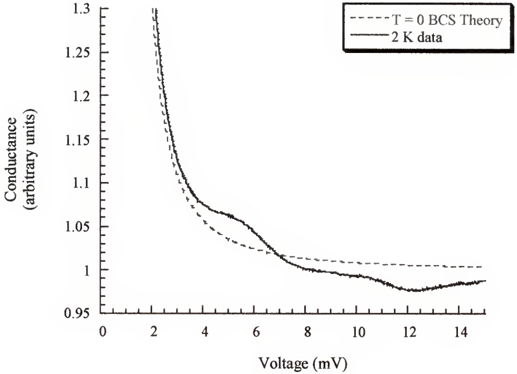

Figure 6.6: Normalized conductance vs. voltage measurements at 2 K. The experimentally determined gap voltage of 1.30 mV was used in the T = 0 BCS calculation, shown by the dashed curve. The expected phonon modes centered at 7 mV and 11 mV are observed.

## 6.3 $La_{0.67}Ca_{0.33}MnO_3$ Tunneling Results

### 6.3.1 Zero-Bias Conductance Measurements

Zero-bias conductance measurements were taken as a function of temperature upon cooling, as shown in figure 6.7. Data were taken from room temperature to 4 K. No hysteresis is found upon warming, indicating temperature stability. The zero-bias conductance is a measure of the density of states at the Fermi level, where barrier effects related to increasing bias voltage are not present. As the temperature is decreased from 300 K, the tunneling conductance decreases, reaching a minimum at approximately 250 K, corresponding to the resistance maximum with temperature. As the temperature continues to decrease, the tunneling conductance increases slowly, while the resistivity reduction is significantly larger as the material undergoes the metal-insulator transition.

This type of conductance spectra suggests that during the ferromagnetic transition, the Fermi level moves through a mobility edge between localized and extended electronic states. Such behavior has been seen in similar metal-insulator systems, including systems with ferromagnetic order, such as $Gd_{3-x}v_xS_4$.[46] It is possible the localized and extended states may both be polaronic, with different mobilities and sizes, although the zero bias conductance data by itself can not distinguish between polaronic and non-polaronic mechanisms leading to mobility induced metal-insulator transitions. The transport in this system therefore is dominated by the characteristics of the state, whether they are mobile or localized, rather than the absolute density.

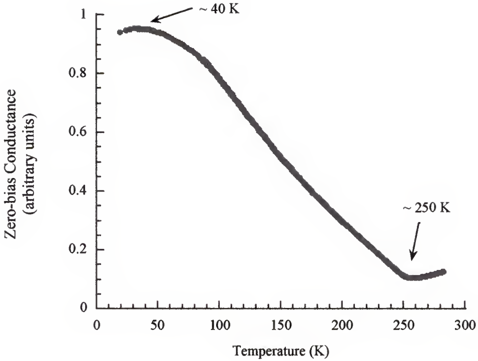

Figure 6.7: Typical zero-bias tunneling conductance data as a function of temperature for an $La_{0.67}Ca_{0.33}MnO_3$ tunnel junction.

As the temperature is further reduced, a maximum in the tunneling conductance is seen at approximately 40 K. Figure 6.8 focuses on this turnover for a different $La_{0.67}Ca_{0.33}MnO_3$ tunnel junction. Higher quality junctions show a more pronounced tunneling conductance maxima at ~ 40 K. The decrease in the conductance below 40 K implies a depletion in the density of states of the Fermi level of the manganite film. The sharp drop in conductance at ~7.2 K is associated with the gap of the superconducting Pb electrode. At $T = \frac{T_c}{2} = 20$ K, the conductance is reduced by only 7%, making it unlikely that an isotropic gap exists over the whole Fermi surface. The reduction in the conductance at the Fermi level is consistent with the transfer of spectral weight from one spin band to another.

To better characterize the density of electronic states of the manganite thin film, conductance spectra are obtained for temperatures above the $T_c$ of Pb, where the Pb electrode is a normal metal with a constant density of states. A typical, unnormalized conductance data set is show in figure 6.9 for a temperature range of 2 K to 265 K. The measurements always yield a conductance that is linear with applied voltage at low temperature, becoming quadratic as the temperature is increased towards $T_c$. The linear background becomes sharper with decreasing temperature. A large linear conductance background over a bias range of hundreds of mV is not a unique feature of the manganites. Linear backgrounds have previously been observed in a wide variety of tunneling systems, including high-$T_c$ cuprate compounds, Al-$Al_2O_3$-Pb, and Cr-$Cr_2O_3$-Pb junctions.[48] These features have been observed in Sr-doped ferromagnetic manganite

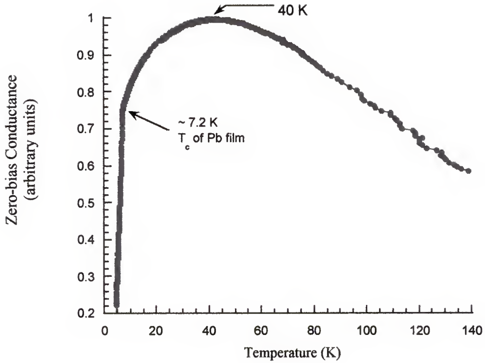

Figure 6.8: Zero-bias tunneling conductance vs. temperature of a $La_{0.67}Ca_{0.33}MnO_3$ film. This second sample focuses on the turnover at ~ 40 K. The sharp drop in conductance at ~ 7.2 K is due to the onset of superconductivity of the Pb electrode .

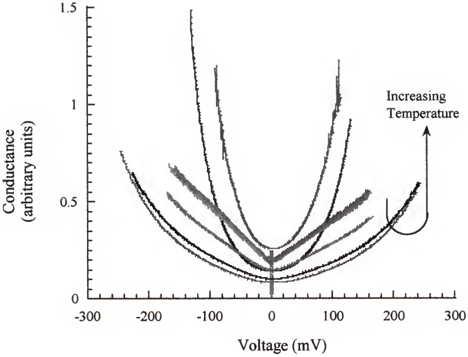

Figure 6.9: Full temperature spectrum of the unnormalized $La_{1-x}Ca_xMnO_3$ tunneling conductance as a function of applied biasing voltage. Temperature ranged from 2 K - 265 K.

films as well as other perovskite materials such as the high-Tc cuprates and bismithates.[49-50] To better understand and explain these remarkable data it is necessary to break up the measurements into several different temperature regimes.

### 6.3.2 Low Temperature Conductance Measurements

We begin by focusing on the low temperature data. A plot of conductance for temperatures between 8 K and 30 K is shown in figure 6.10. Below 40 K the tunneling data show a depletion in the density of states with decreasing temperature. The depletion is centered at the Fermi level and occurs over an energy range of ~ 3.5 meV. The linear background makes it difficult to obtain a true value of the gap. In figure 6.11, low temperature conductance data are normalized to the high-bias ($V > 100$ meV) data taken at 40 K, in an attempt to remove the linear background and to accentuate any changes in the tunneling conductance due to temperature. The data are then scaled to enforce a sum rule, meaning all the missing states at low bias reappear at higher energies over an extended energy range. Therefore, the area under the conductance curve is conserved.

This depletion in the density of states can also be seen in the resistivity of the manganite film. Low temperature electrical transport measurements conducted by Jaime et al. show a $T^2$ temperature dependence above 50 K that vanishes at lower temperatures.[22] The $T^2$ contribution is often ascribed to electron-electron scattering as described in section 4.1.1. However, these authors purport that the $T^2$ dependence is consistent with thermally-activated single-magnon scattering processes, and the disappearance of this would indicate the collapse of the minority spin band as the local spins align with the magnetization.

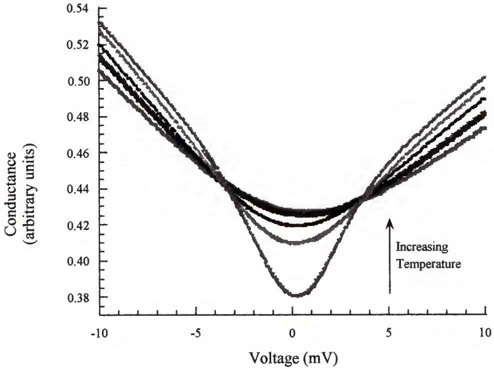

Figure 6.10: Unnormalized conductance vs. voltage for a $La_{0.67}Ca_{0.33}MnO_3$ tunnel junction. Temperatures of 8.6 K, 15.3 K, 20.1 K, 25.2 K, and 30.0 K are shown. A small depletion in the density of states with decreasing temperature is centered at the Fermi level with a width of ~ 3.5 meV.

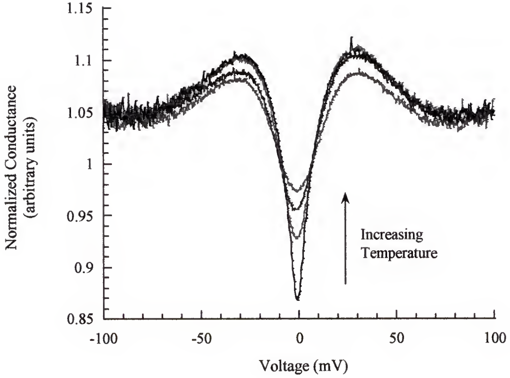

Figure 6.11: Normalized low temperature conductance vs. voltage for a $La_{0.67}Ca_{0.33}MnO_3$ tunnel junction. The data have been normalized to the 40 K high-bias conductance data and scaled to enforce a sum rule. Temperatures of 10.4 K, 17.5 K, 24.2 K, and 39.5 K are shown.

As discussed in chapter 3, recent band structure calculations indicate that the manganites are nearly half-metallic, with a spin gap opening at low temperatures. The opening of a spin gap would localize the minority carriers below the mobility edge. Either explanation would explain the depletion in the density of states observed in our measurements.

### 6.3.3 Middle Temperature Conductance Measurements

The middle temperature range data, from 35 K to 80 K, are shown in figure 6.12. Increasing temperature lowers the conductance curves, as expected from the zero-bias conductance data. Superimposed on the background conductance is an inelastic excitation, seen in the high-bias ($V > 100$ mV) data as small changes in the conductance. Removing the linear background allows us to show these inelastic excitations seen in the density of states over a broad energy range as shown in figure 6.13. As the temperature is increased toward the transition temperature, the amplitude of the inelastic excitations increases and shifts to lower energy. Notice that these excitations produced only a 1% change in the total conductance at low temperatures.

Possible explanations for the inelastic excitations include phonons, magnetic excitations, and polarons. It is unlikely that the excitations are due to phonons since the observed energy of the excitation, ~ 230 meV, is substantially larger than the energy of any crystal mode with significant spectral weight. If we associate the inelastic excitations as an inelastic coupling of the conduction electrons to the long range magnetic interactions then the amplitude of the inelastic excitations should increase as the magnetism develops with decreasing temperature. However, the opposite is

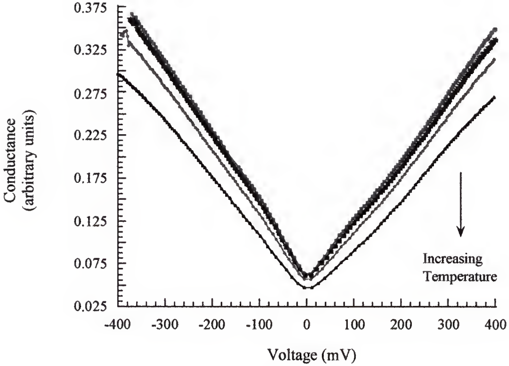

Figure 6.12: Unnormalized $La_{0.67}Ca_{0.33}MnO_3$ conductance vs. voltage for temperatures ranging from 33 K to 80 K. Small changes in the conductance can be seen at high bias (V > 100 mV). Actual temperatures shown are 33.7 K, 42.9 K, 58.0 K, and 79.2 K.

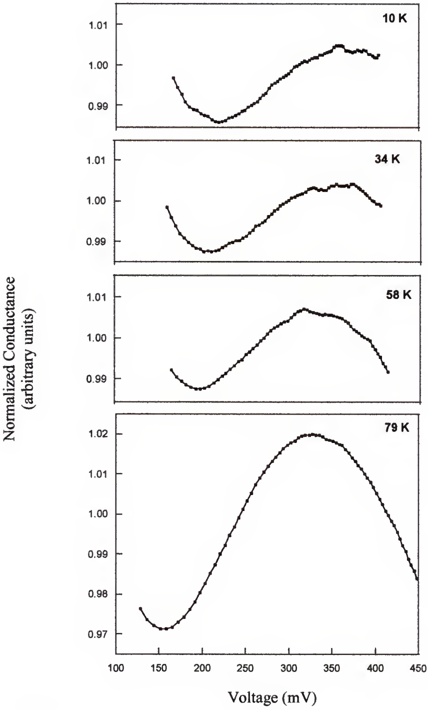

Figure 6.13: Normalized $La_{0.67}Ca_{0.33}MnO_3$ conductance vs. voltage measurements. The linear background has been removed from the data. Inelastic excitations increase in amplitude with increasing temperature. The excitation energy is ~ 230 meV.

observed, which rules out this possibility. We believe these excitations are due to inelastic coupling of the conduction electrons to localized carriers. Support for this picture comes from thermopower measurements which show a polaron formation of characteristic energy of ~ 200 meV below the $T_c$ of the material.[51] This energy is essentially the same as observed from the tunneling inelastic excitations, indicating that the excitations may be evidence of polaronically localized electrons which persist even at low temperatures. This interpretation is further supported by Raman scattering measurements. These measurements can be successfully modeled as polaronically localized states with similar formation energy.[31]

### 6.3.4 High Temperature Conductance Measurements

As the temperature continues to increase, the background conductance becomes more parabolic, as shown in figure 6.14. Room temperature conductance measurements, not shown here, are basically flat. The change in the background conductance is attributed mostly to barrier effects.

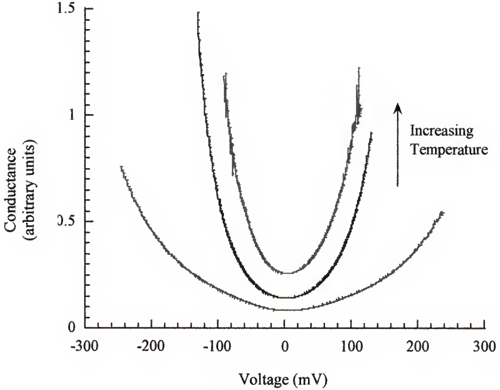

Figure 6.14: Unnormalized $La_{0.67}Ca_{0.33}MnO_3$ conductance measurements as a function of applied voltage for temperatures of 150 K, 242 K, and 265 K. Note the background conductance becomes more parabolic with increasing temperature.

## 6.4 Preliminary $La_{0.67}Sr_{0.33}MnO_3$ Tunneling Results

Preliminary tunneling measurements have been conducted on $La_{0.67}Sr_{0.33}MnO_3$ thin film samples using the same ion-milling processing techniques described in chapter 5. $La_{1-x}Sr_xMnO_3$ films in general are rougher than $La_{1-x}Ca_xMnO_3$ films, making it more difficult to form high-quality junctions. The junctions presented here have a $\delta R \sim 5$.

### 6.4.1 Zero-Bias Conductance Measurements

The $La_{0.67}Sr_{0.33}MnO_3$ zero-bias conductance measurements (figure 6.15) show a peak in the conductance at ~ 30 K, similar to the peak found at ~ 40 K for $La_{0.67}Ca0_{.33}MnO_3$ samples. As discussed for the $La_{0.67}Ca_{0.33}MnO_3$ junctions, these data indicate a slowly increasing density of states with decreasing temperature below $T_c$. As the temperature is reduced, the states evolve from being localized to extended, and transport is dominated by mobility and scattering effects. At ~ 30 K there appears to be a depletion in the density of electronic states with decreasing temperature.

Figure 6.16 shows unnormalized conductance spectra of a $La_{0.67}Sr_{0.33}MnO_3$ tunnel junction for temperatures ranging from ~ 10 K - 250 K. A low-bias linear background and an exponentially dependent high-bias background are observed, indicating that a Schottky-like barrier is also present in these samples. The background becomes more parabolic with increasing temperature, which again is attributed to a barrier effect as for the Ca-doped films.

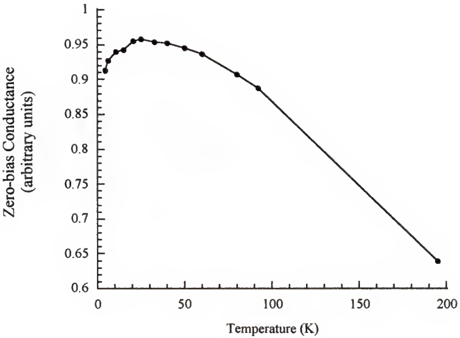

Figure 6.15: Zero-bias $La_{0.67}Sr_{0.33}MnO_3$ conductance measurements as a function of temperature. The solid curve is a guide to the eye. A depletion in the conductance with decreasing temperature is seen below ~ 30 K.

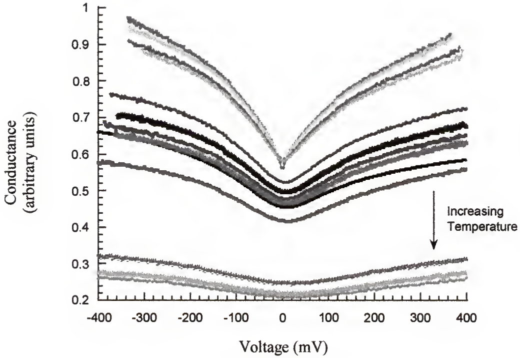

Figure 6.16: Unnormalized $La_{0.67}Sr_{0.33}MnO_3$ conductance vs. voltage for T = 10 K – 250 K. Note the linear background becomes more parabolic with increasing temperature.

### 6.4.2 Low Temperature Measurements

The low temperature measurements reveal a depletion in the density of states below ~ 30 K, as shown in figure 6.17. Although more data need to be taken, it is clear that a depletion in the density of states below a few millivolts exists. The junction quality is not high enough to see the expected high-bias deviations in the conductance over a broad energy range associated with inelastic excitations. However, it is evident that qualitatively similar features exist between the $La_{0.67}Ca_{0.33}MnO_3$ and $La_{0.67}Sr_{0.33}MnO_3$ tunneling characteristics.

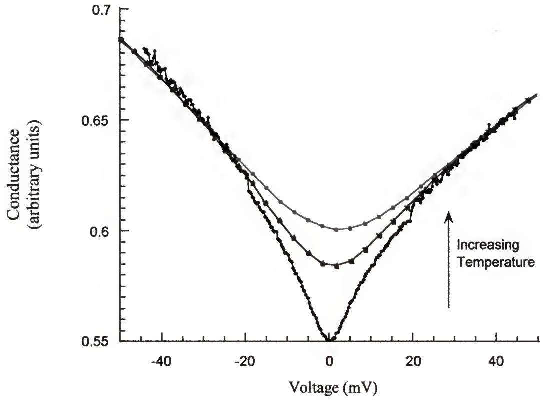

Figure 6.17: Unnormalized $La_{0.67}Sr_{0.33}MnO_3$ conductance vs. applied voltage. A small depletion in the density of states centered at the Fermi level and extending a few millivolts is seen. Temperatures of 10 K, 15K, and 30 K are shown. The solid curves are guides for the eye.

# CHAPTER 7
# SUMMARY

The experimental work presented in this dissertation attempts to measure the density of electronic states of the ferromagnetic lanthanum manganites. Thin film samples of $La_{0.67}Ca_{0.33}MnO_3$ and $La_{0.67}Sr_{0.33}MnO_3$ were used to fabricate tunnel junctions using two separate methods to produce high-quality insulating barriers. Measurements of current and conductance as a function of applied voltage were taken for temperatures ranging from 2 K to 300 K.

The present tunneling results are consistent with other experimental results including transport, Raman spectroscopy, and thermopower measurements. The double exchange mechanism, first proposed by Zener, provides a model both for its conductivity and ferromagnetic ordering. Electron transport in these materials is controlled by polaronic formation, where in the insulating phase, small localized polarons dominate. For the $La_{0.67}Ca_{0.33}MnO_3$ samples, the tunneling measurements show a density of electronic states that increases slowly with decreasing temperature below 250 K, the ferromagnetic ordering temperature of the $La_{0.67}Ca_{0.33}MnO_3$ film. Below the transition, the large change in the resistivity of the material is accompanied by only a small change in the density of states at the Fermi level. Our measurements are consistent with a Fermi level moving through a mobility edge to a region of extended states as this material ferromagnetically orders.

Below 40 K, a depletion in the density of states at the Fermi level with decreasing temperature is observed. This result is consistent with a transfer of spectral weight from a minority spin band to the majority spin band. Similar conclusions have been drawn by transport measurements, attributing the $T^2$ behavior in resistivity to magnon scattering processes. The data is supported by recent theoretical calculations indicating that for temperatures substantially below $T_c$, a minority spin band persists, and that true half-metallic behavior may not exist even at $T = 0$.

In addition, evidence exists for inelastic excitations in the density of states over a broad energy range. These excitations are revealed as small changes (less than 1% at low temperatures) in the density of states in the $La_{0.67}Ca_{0.33}MnO_3$ tunneling spectroscopy data and extend over an bias range of approximately half a volt. Raman studies find a polaron formation energy in the same energy range as observed from the tunneling results. These inelastic excitations may be evidence of polaronically localized electrons coexisting with mobile carriers at temperatures well below the ordering temperature.

The $La_{0.67}Sr_{0.33}MnO_3$ tunneling characteristics are consistent with the $La_{0.67}Ca_{0.33}MnO_3$ tunneling results in that they both show a density of electronic states that increases slowly with decreasing temperature and a depletion in the density of states at the Fermi level below ~ 30 K. Although no inelastic excitations are seen in the $La_{0.67}Sr_{0.33}MnO_3$ tunneling data, the quality of the junctions are not high enough to observe such small deviations.

Finally, it should be noted that similar behavior is seen in other semiconducting systems where the ferromagnetic ordering determines the transport properties of the material.

# REFERENCES

1 R. von Helmolt, J. Wecker, B. Holzapfel, L. Schultz, and K. Samwer, Phys. Rev. Lett. **71** (14), 2331 (1993).

2 S. Jin, M. McCormack, T.H. Tiefel, and R. Ramesh, J. Appl. Phys. **76**, 6929 (1994).

3 C. Zener, Phys. Rev. **82** (3), 403 (1951).

4 P.W. Anderson and H. Hasegawa, Phys. Rev. **100** (2), 675 (1955).

5 P.G. de Gennes, Phys. Rev. **118** (1), 141 (1960).

6 A.J. Millis, P.B. Littlewood, and B.I. Shraiman, Phys. Rev. Lett. **74** (25), 5144 (1995).

7 A.J. Millis, B.I. Shraiman, and R. Mueller, Phys. Rev. Lett. **77** (1), 175 (1996).

8 H. Röder, Jun Zang and A.R. Bishop, Phys. Rev. Lett. **76** (8), 1356 (1996).

9 A.J. Millis, T. Darling, and A. Migliori, J. Appl. Phys. **83** (3), 1588 (1997).

10 I. Giaever, Phys. Rev. Lett. **5**, 157 (1960).

11 E.L. Wolf, *Principles of Electron Tunneling Spectroscopy.* Oxford University Press, Oxford, 1985.

12 W.F. Brinkman, R.C. Dynes, and J.M. Rowell, J. Appl. Phys. **41** (5), 1915 (1970).

13 J.B. Goodenough, J. Appl. Phys. **81** (8), 5330 (1997).

14 Jonker and van Santeen, Physica **16**, 337 (1950).

15 P. Schiffer, A.P. Ramierez, W. Bao, and S.-W. Cheong, Phys. Rev. Lett. **75** (18), 3336 (1995).

16 A.J. Millis, Nature **392**, 147 (1998).

17 A.P. Ramierz, J. Phys: Condens. Matter **9**, 8171 (1997).

18 M. Winter, http:\\www.webelements.com, University of Sheffield, England (1999).

19 J. Blasco, J. García, J.M. de Teresa, M.R. Ibarra, J. Perez, P.A. Algarabel, C.Marquina, and C. Ritter, Phy. Rev. B **55** (14), 8905 (1997).

20 J. B. Goodenough, Phys. Rev. **100** (2), 564 (1955).

21 H. Kubo and N. Ohata, J. Phys. Soc. Jpn. **33**, 21 (1972).

22 M. Jaime, P. Lin, M.B. Salamon, and P.D. Han, Phys. Rev. B **58** (10), R5901 (1998).

23 W.E. Pickett and D.J. Singh, Phys. Rev. B **55** (14), R8642 (1997).

24 M. Jaime, M.B. Salamon, K. Pettit, M, Rubinstein, R.E. Treece, J. S. Horwitz, and D.B Chrisey, Appl. Phys. Lett. **68** (11), 1576 (1996).

25 W. Archibald, J.-S. Zhou, and J.B. Goodenough, Phys. Rev. B **53** (21), 14445 (1996).

26 B.F. Woodfield, M.L. Wilson, and J.M. Byers, Phys. Rev. Lett. **78** (16), 3201 (1997).

27 C. Kittel, *Introduction to Solid State Physics*, 6th ed. Wiley, New York, 1986.

28 J.L. Cohn, J.J. Neumier, C.P. Popoviciu, K.J. McClellan, and Th. Leventouri, Phys. Rev. B **56** (14), R8495 (1997).

29 G.-M. Zhao, K. Conder, H. Keller, and K.A. Muller, Nature **381**, 676 (1996).

30 Q. Huang, A. Santoro, J.W. Lynn, R.W. Erwin, J.A. Borchers, J.L. Peng, K. Ghosh, and R.L. Greene, Phys. Rev. B **58** (5), 2684 (1998).

31 S. Yoon, H.L. Liu, G. Schollerer, S.L. Cooper, P.D. Han, D.A. Payne, S.-W. Cheong, and Z. Fisk, Phys. Rev. B **58** (5), 2795 (1998).

32 M. Quijada, J. Cerne, J.R. Simpson, H.D. Drew, K.H. Ahn, A.J. Millis, R. Shreekala, R. Ramesh, M. Rajeswari, and T. Venkatesan, Phys. Rev. B **58** (24), 16093 (1998).

33 C.H. Booth, F. Bridges, G. H. Kwei, J.M. Lawrence, A.L. Cornelius and J.J. Neumeier, Phys. Rev. Lett. **80** (4), 853 (1998).

34 T.A. Tyson, J. Mustre de Leon, S.D. Conradson, A.R. Bishop, J.J. Neumeier, H. Röder, and Jun Zang, Phys. Rev. B **53** (21), 13 985 (1996).

35 J.W. Lynn, R.W. Erwin, J.A. Borchers, A. Santoro, Q. Huang, J.-L. Peng, and R.L. Greene, J. Appl. Phys. **81** (8), 5488 (1997).

36 J.W. Lynn, R.W. Erwin, J.A. Borchers, Q. Huang, A. Santoro, J.-L. Peng, and Z. Y. Li, Phys. Rev. Lett. **76** (21), 4046 (1996).

37 C.P. Adams, J.W. Lynn, Y.M. Mukovskii, A.A. Arsenov, and D.A. Shulyatev, preprint.

38 S.J.L. Billinge, R.G. DiFrancesco, G.H. Kwei, J.J. Neumeier, and J.D. Thompson, Phys. Rev. Lett. **77** (4), 715 (1996).

39 D. Louca, T. Egami, E.L. Brosha, H. Röder, and A.R. Bishop, Phys. Rev. B **56** (14), R8475 (1997).

40 J.Y.T. Wei, N.-C. Yeh, and R.P. Vasquez, Phys. Rev. Lett., **79** (25), 5150 (1997).

41 M. Fäth, "Scanning Tunneling Spectroscopy on Correlated Electron Systems," Ph.D. dissertation, Leiden (1999).

42 Y. Lu, X.W. Li, G.Q. Gong, Gang Xiao, A. Gupta, P. Lecoeur, J.Z. Sun, Y.Y. Wang, and V.P. Dravid, Phys. Rev. B, **54** (12), R8357 (1996).

43 J.Z. Sun, L. Krusin-Elbaum, A. Gupta, Gang Xiao, P.R. Duncombe, and S.S.P. Parkin, IBM J. Res. Develop. **42**, 89 (1998).

44 M. Gurvitch, J.M. Valles, R.C. Dynes, A.M. Cucolo, and L.F. Schneemeyer, Physica C **162-164**, 1067 (1989).

45 H.R. Kauffman, *Fundamentals of Ion-Source Operation*, Commonwealth Scientific Corporation, Alexandria, VA 1984.

46 W.A. Thompson and S. von Molnar, J. Appl. Phys. **41** (13), 5218 (1970).

47 S. von Molnar and T. Penny, *Localization and Metal-Insulator Transitions*, ed. by H. Fritzche and D. Adler, Plenum, New York 1985. sec. "Transitions The Mott Mobility Edge and the Magnetic Polaron."

48 J.R. Kirtley, D.J. Scalapino, Phys. Rev. Lett. **65** (6), 798 (1990).

49 M. Gurvitch, J.M. Valles, Jr., A.M. Cucolo, R.C. Dynes, J.P. Garno, L.F. Schneemeyer, and J.V. Waszczak, Phys. Rev. Lett. **63** (9), 1008 (1989).

50 F. Sharifi, A. Pargellis, and R.C. Dynes, Phys. Rev. Lett. **64** (4), 509 (1991).

51 M. Jaime, M.B. Salamon, M. Rubinstein, R.E. Treece, J.S. Horwitz, and D.B. Chrisey, Phys. Rev. B **54** (17), 11914 (1996).

# BIOGRAPHICAL SKETCH

Heather Diane Lynn was born the youngest child of Dr. Jeffrey W. and Linda M. Lynn on March 17, 1972 in Oak Ridge, Tennessee. She attributes her early interest in science to her parents, whose own passion for science and nature opened her eyes to a world of discovery. The summer before her senior year in high school she participated in her first science and engineering research program at the Naval Surface Warfare Center in White Oak, Maryland, under the guidance of Dr. Mark Spano. Her studies included magnetostriction experiments on $(Tb_xDy_{1-x})_{80}Gd_{20}$ single crystals. Success in the program, including being an author on her first scientific paper published in the Journal of Applied Physics, cemented her love for the field. After Heather graduated from Paint Branch High School in Burtonsville, Maryland, in the spring of 1990, she immediately went to a two-week science program sponsored by the Department of Energy at Argonne National Laboratory in Chicago, Illinois. She finished that summer continuing her studies at White Oak and produced a second published paper. While attending the University of Maryland in College Park, Maryland, Heather worked at the National Institute of Standards and Technology in Gaithersburg, Maryland, in the radiometric physics division. She also worked at the University of Maryland Center for Superconductivity Research. As a participant in the Department of Energy Science and Engineering Research Semester, Heather spent the spring semester of her junior year at Los Alamos National Laboratory in Los Alamos, New Mexico in the accelerator technology division. During this program Heather met her future husband, Quentin Hudspeth. For the next two summers, she continued working at Los Alamos in the neutron scattering center under Dr. Joyce Goldstone. In the spring of 1994, after four years in college, Heather graduated with a B.S. with honors in physics. The following fall she began her graduate studies at the University of Florida in physics. In the summer of 1995, she married her wonderful husband, Quentin. The next spring, she joined the research group under Dr. Fred Sharifi, beginning the work of which this dissertation is the culmination. Besides the work described in this dissertation, she also took the opportunity to learn techniques for writing small structures using a scanning electron microscope.

I certify that I have read this study and that in my opinion it conforms to acceptable standards of scholarly presentation and is fully adequate, in scope and quality, as a dissertation for the degree of Doctor of Philosophy.

Fred Sharifi

Fred Sharifi, Chairman
Associate Professor of Physics

I certify that I have read this study and that in my opinion it conforms to acceptable standards of scholarly presentation and is fully adequate, in scope and quality, as a dissertation for the degree of Doctor of Philosophy.

Selman P. Hershfield

Selman P. Hershfield
Associate Professor of Physics

I certify that I have read this study and that in my opinion it conforms to acceptable standards of scholarly presentation and is fully adequate, in scope and quality, as a dissertation for the degree of Doctor of Philosophy.

Arthur F. Hebard

Arthur F. Hebard
Professor of Physics

I certify that I have read this study and that in my opinion it conforms to acceptable standards of scholarly presentation and is fully adequate, in scope and quality, as a dissertation for the degree of Doctor of Philosophy.

Christopher J. Stanton

Christopher J. Stanton
Professor of Physics

I certify that I have read this study and that in my opinion it conforms to acceptable standards of scholarly presentation and is fully adequate, in scope and quality, as a dissertation for the degree of Doctor of Philosophy.

Stephen J. Pearton
Professor of Materials Science and Engineering

This dissertation was submitted to the Graduate Faculty of the Department of Physics in the College of Liberal Arts and Sciences and to the Graduate School and was accepted as partial fulfillment of the requirements for the degree of Doctor of Philosophy.

May 2000

Dean, Graduate School